

**Mechano-chemical synthesis of amorphous manganese borohydride, the effect  
of catalytic additives on its hydrogen generation properties, and  
crystallization during solvent extraction**

by

Deepak Kini Mattar

A thesis  
presented to the University of Waterloo  
in fulfillment of the  
thesis requirement for the degree of  
Master of Applied Science  
in  
Mechanical Engineering

Waterloo, Ontario, Canada, 2016

© Deepak Kini Mattar 2016

## **Author's Declaration**

I hereby declare that I am the sole author of this thesis. This is a true copy of the thesis, including any required final revisions, as accepted by my examiners.

I understand that my thesis may be made electronically available to the public.

## Abstract

This thesis forms one of the final parts of an extended study on the hydrogen storage and generation properties of metal borohydrides.

Manganese borohydride,  $\text{Mn}(\text{BH}_4)_2$ , which is expected to be formed by the mechano-chemical activation synthesis (MCAS) from a mixture of sodium borohydride,  $\text{NaBH}_4$ , and manganese chloride,  $\text{MnCl}_2$ , is the candidate explored in this thesis. The effect of catalytic additives graphene and ultrafine filamentary carbonyl nickel (Ni), in addition to lithium amide ( $\text{LiNH}_2$ ) is also studied.

The mixture of ( $2\text{NaBH}_4 + \text{MnCl}_2$ ) was ball milled in a magneto-mill. No gas release was detected. The XRD patterns of the ball milled mixture exhibit only the Bragg diffraction peaks of NaCl-type salt which on the basis of the X-ray diffraction results reported in the literature is possibly identified as a solid solution  $\text{Na}(\text{Cl})_x(\text{BH}_4)_{(1-x)}$ , possessing a cubic NaCl-type crystalline structure. No presence of any crystalline hydride was detected by powder X-ray diffraction which clearly shows that  $\text{NaBH}_4$  in the initial mixture must have reacted with  $\text{MnCl}_2$  forming a NaCl-type by-product and another hydride that does not exhibit X-ray Bragg diffraction peaks. Mass spectrometry (MS) of gas released from the ball milled mixture during combined thermogravimetric analysis/differential scanning calorimetry (TGA/DSC) experiments, confirms mainly hydrogen ( $\text{H}_2$ ) with a small quantity of diborane gas,  $\text{B}_2\text{H}_6$ . The Fourier transform infra-red (FT-IR) spectrum of the ball milled ( $2\text{NaBH}_4 + \text{MnCl}_2$ ) is similar to the FT-IR spectrum of crystalline manganese borohydride,  $c\text{-Mn}(\text{BH}_4)_2$ , synthesized by ball milling which strongly suggests that an amorphous  $a\text{-Mn}(\text{BH}_4)_2$  hydride was formed.

The catalytic additives of 5 wt. % graphene and ultrafine filamentary nickel added before ball milling significantly improved the dehydrogenation characteristics of the mixture. The addition of graphene suppressed the formation of  $B_2H_6$ . The powder mixture desorbed ~3 wt. %  $H_2$  after 24 hours at  $120^\circ C$ .

5 wt. % lithium amide,  $LiNH_2$ , when added before ball milling changed the nature of the dehydrogenation reaction from endothermic to exothermic and almost completely eliminated the release of diborane. This powder mixture desorbed ~3 wt. %  $H_2$  after 24 hours at  $140^\circ C$ .

The highlight of this work is the crystallization of likely amorphous  $Mn(BH_4)_2$  produced after MCAS without additives during the subsequent filtration/extraction process and the generation of ~7.5 wt. % of  $H_2$  by this powder, which has never before been reported in literature.

## **Acknowledgments**

This research was supported by the Natural Sciences and Engineering Research Council of Canada (NSERC) Discovery grant.

The FT-IR measurements were conducted by Dr. S.A. Kornic from the Department of Chemistry and Chemical Biology, McMaster University, Hamilton, Ontario, Canada.

I would like to thank Dr. Marek Polanski for his help with the thermal analysis of the prepared samples and Prof. Linda Nazar for use of the XRD equipment.

The solvent extraction method used in this thesis was first proposed by Dr. Mazda Biglari, and his idea is gratefully acknowledged.

I would also like to thank Dr. John Shu of CNEM Corporation (Canada) for donating ultrafine filamentary carbonyl nickel (Ni) powders and Dr. Les Stobinski of the Warsaw University of Technology Graphene Laboratory for donating reduced graphene oxide/graphene.

Amirreza Shirani Bidabadi was instrumental in assisting me with the completion of this work, and I thank him for being my guiding light and mentor during my time at the University of Waterloo.

Prof. Robert Varin, thank you for your guidance, encouragement and continued support throughout my studies.

## **Dedication**

To my parents: thank you for being there every step of the way, through all the twists and turns, and the crests and troughs of life.

"Always hopeful, yet discontent. [He knows] Changes aren't permanent - but change is." - Neil Peart

## Table of Contents

<b>1</b>	<b>Introduction</b> .....	<b>1</b>
1.1	Motivation.....	1
1.2	Hydrogen Storage Methods for Mobile Applications.....	1
1.2.1	High-pressure tanks.....	2
1.2.2	Cryogenic storage.....	2
1.2.3	Solid State Hydrides.....	2
1.3	US Department of Energy (DOE) Targets.....	3
1.4	Previous work.....	6
1.5	Statement of Objectives.....	8
<b>2</b>	<b>Experimental Procedure</b> .....	<b>10</b>
2.1	Sample Preparation.....	10
2.2	Milling energy input and milling mode.....	12
2.3	Solvent extraction.....	12
2.4	Measurement of H <sub>2</sub> desorption.....	13
2.5	X-ray Diffraction (XRD), SEM and FT-IR analysis.....	15
2.6	DSC and TGA analysis.....	16
2.7	Improvisation of solvent extraction process.....	17
<b>3</b>	<b>Results and Discussion</b> .....	<b>20</b>
3.1	Characterization of morphology and microstructure of the ball-milled samples.....	20
3.2	Characterization of morphology and microstructure of ball-milled samples with catalytic additives.....	29
3.3	Characterization of morphology and microstructure of ball-milled samples doped with 5 wt. % LiNH <sub>2</sub> .....	31
3.4	Isothermal dehydrogenation behavior of ball-milled samples.....	34
3.5	Isothermal dehydrogenation behavior of ball-milled samples with catalytic additives.....	37
3.6	Isothermal dehydrogenation of ball-milled samples doped with LiNH <sub>2</sub> .....	40
3.7	Thermal (thermodynamic) behaviour of ball milled samples in DSC/TGA and gas mass spectrometry (MS).....	41
3.8	Thermal (thermodynamic) behaviour of ball milled samples with graphene additive in DSC/TGA and gas mass spectrometry (MS).....	44
3.9	Thermal (thermodynamic) behaviour of ball milled samples with LiNH <sub>2</sub> additive in DSC/TGA and gas mass spectrometry (MS).....	46
3.10	Microstructure of crystalline Mn(BH <sub>4</sub> ) <sub>2</sub> produced by solvent extraction/filtration....	47
3.11	Isothermal dehydrogenation behavior of the extracted sample.....	51
3.12	Thermal (thermodynamic) behaviour of ball milled samples with LiNH <sub>2</sub> additive in DSC/TGA and gas mass spectrometry (MS).....	52

<b>4</b>	<b>Conclusions.....</b>	<b>54</b>
	<b>References.....</b>	<b>56</b>
	<b>Appendix A: Conversion of Volumetric Sieverts Apparatus Measurement to wt. %.....</b>	<b>60</b>
	<b>Appendix B: Collection of SEM Images.....</b>	<b>61</b>
	<b>Appendix C: DSC/TGA and MS data reproducibility.....</b>	<b>67</b>
	<b>Appendix D: Enthalpy of Reactions (5) and (6).....</b>	<b>68</b>
	<b>Appendix E: Hydrogen/diborane peak ratios of all samples up to 200°C.....</b>	<b>69</b>
	<b>Publications as a result of this work.....</b>	<b>70</b>

## List of Figures

<b>Figure 1:</b> Schematic of solvent extraction process used in this work for separation of $\text{Mn}(\text{BH}_4)_2$ from the mixture with $\text{NaCl}$ .....	13
<b>Figure 2:</b> Schematic of the improved extraction process to remove $\text{NaCl}$ from a mixture of $\text{Mn}(\text{BH}_4)_2$ and $\text{NaCl}$ .....	18
<b>Figure 3:</b> SEM micrographs of as received $\text{NaBH}_4$ (a) lower magnification and (b) higher magnification.....	20
<b>Figure 4:</b> SEM micrographs of as received $\text{MnCl}_2$ [20] (a) lower magnification and (b) higher magnification.....	21
<b>Figure 5:</b> SEM micrographs of $2\text{NaBH}_4+\text{MnCl}_2$ 0.5 h BM ( $Q_{\text{TR}}=36.4$ kJ/g) (a) lower magnification and (b) higher magnification.....	21
<b>Figure 6:</b> SEM micrographs of $\text{NaBH}_4+\text{MnCl}_2$ 5 h BM ( $Q_{\text{TR}}=364$ kJ/g) (a) lower magnification and (b) higher magnification.....	22
<b>Figure 7:</b> XRD patterns for the $(2\text{NaBH}_4+\text{MnCl}_2)$ mixture ball milled for 0.5 h ( $Q_{\text{TR}}=36.4$ kJ/g), 1 h ( $Q_{\text{TR}}=72.8$ kJ/g) and 5 h ( $Q_{\text{TR}}=364$ kJ/g).....	23
<b>Figure 8:</b> Enlargement of the (200) $\text{NaCl}$ peak (100% intensity) in comparison to the (200) standard diffraction line from the ICDD PDF#(05-0628).....	24
<b>Figure 9:</b> (a) FT-IR spectrum for a $(2\text{NaBH}_4+\text{MnCl}_2)$ sample ball milled for 5 h ( $Q_{\text{TR}}=364$ kJ/g). (b) Reference FT-IR spectrum for a $(2\text{LiBH}_4+\text{MnCl}_2)$ sample ball milled for 2 h ( $Q_{\text{TR}}=145.6$ kJ/g) containing a synthesized, crystalline $\text{Mn}(\text{BH}_4)_2$ hydride (adopted from [16, 18]).....	26
<b>Figure 10:</b> SEM images of (a) Filamentary nickel N04 and (b) graphene.....	29
<b>Figure 11:</b> SEM micrographs of $(2\text{NaBH}_4+\text{MnCl}_2)+5\text{wt.}\%$ graphene 0.5 h BM ( $Q_{\text{TR}}=36.4$ kJ/g) (a) lower magnification (b) higher magnification.....	30
<b>Figure 12:</b> SEM micrographs of $(2\text{NaBH}_4+\text{MnCl}_2)+5\text{wt.}\%$ Ni 0.5 h BM ( $Q_{\text{TR}}=36.4$ kJ/g) (a) lower magnification (b) higher magnification.....	30
<b>Figure 13:</b> XRD patterns for the $(2\text{NaBH}_4+\text{MnCl}_2)+5\text{wt.}\%$ Ni mixture ball milled for 1 h ( $Q_{\text{TR}}=72.8$ kJ/g).....	31
<b>Figure 14:</b> Amount of $\text{H}_2$ lost during ball milling of $(2\text{NaBH}_4+\text{MnCl}_2)+5\text{wt.}\%$ $\text{LiNH}_2$ mixture for 0-5 h.....	32

<b>Figure 15:</b> SEM micrograph of (2NaBH <sub>4</sub> +MnCl <sub>2</sub> )+5wt.% LiNH <sub>2</sub> 0.5 h BM (Q <sub>TR</sub> =36.4 kJ/g).....	<b>33</b>
<b>Figure 16:</b> XRD patterns for the (2NaBH <sub>4</sub> +MnCl <sub>2</sub> )+5wt.% LiNH <sub>2</sub> mixture before ball milling, after being ball milled for 0.5 h (Q <sub>TR</sub> =36.4 kJ/g) and 1 h (Q <sub>TR</sub> =72.8 kJ/g), and after desorption at 100°C having been ball milled for 1 h (Q <sub>TR</sub> =72.8 kJ/g).....	<b>34</b>
<b>Figure 17:</b> Desorption curves for the (2NaBH <sub>4</sub> +MnCl <sub>2</sub> ) samples milled with increasing milling energy input Q <sub>TR</sub> for (a) 0.5 h; Q <sub>TR</sub> =36.4 kJ/g, (b) 1 h; Q <sub>TR</sub> =72.8 kJ/g, and (c) 5 h; Q <sub>TR</sub> =364 kJ/g. (d) The Arrhenius plots of rate constant k with temperature for estimation of the apparent activation energy of hydrogen desorption: 1 - 0.5 h BM (Q <sub>TR</sub> =36.4 kJ/g): y= -118.21x+36.016, R <sup>2</sup> =0.9995, 2 - 1 h BM (Q <sub>TR</sub> =72.8 kJ/g): y= -123.09x+37.754; R <sup>2</sup> =0.9867 and 3 - 5 h BM (Q <sub>TR</sub> =364 kJ/g ): y= -177.07x+52.628; R <sup>2</sup> =0.9784.....	<b>35</b>
<b>Figure 18:</b> XRD pattern of the 0.5 h ball milled sample after isothermal dehydrogenation at 120°C for 20.7 h.....	<b>37</b>
<b>Figure 19:</b> Desorption curves for the (2NaBH <sub>4</sub> +MnCl <sub>2</sub> ) samples milled with additives (a) Ni for 0.5 h; Q <sub>TR</sub> =36.4 kJ/g, (b) graphene for 0.5 h; Q <sub>TR</sub> =36.4 kJ/g, and (c) Ni for 1 h; Q <sub>TR</sub> =72.8 kJ/g.....	<b>38</b>
<b>Figure 20:</b> The Arrhenius plots of rate constant k with temperature for estimation of the apparent activation energy of hydrogen desorption (a) 0.5 h BM 5wt.% Ni (Q <sub>TR</sub> =36.4 kJ/g): y= -116.68 + 36.24, R <sup>2</sup> =0.948, (b) 0.5 h BM 5wt.% graphene (Q <sub>TR</sub> =36.4 kJ/g): y=-125.93 + 38.323; R <sup>2</sup> =0.99553 and (c) 1 h BM 5wt.% Ni (Q <sub>TR</sub> =72.8 kJ/g): y= -115.19 + 35.759; R <sup>2</sup> =0.9977.....	<b>39</b>
<b>Figure 21:</b> (a) Desorption curves for the (2NaBH <sub>4</sub> +MnCl <sub>2</sub> )+5wt.% LiNH <sub>2</sub> samples milled for 0.5 h (Q <sub>TR</sub> =36.4 kJ/g); (b) the Arrhenius plots of rate constant k with temperature for estimation of the apparent activation energy of hydrogen desorption for 0.5 h BM, 5 wt.% LiNH <sub>2</sub> (Q <sub>TR</sub> =36.4 kJ/g): y= -55.61 ± 19.269, R <sup>2</sup> =0.967.....	<b>40</b>
<b>Figure 22:</b> (a) Mass spectrometry (MS) gas desorption spectra for a (2NaBH <sub>4</sub> +MnCl <sub>2</sub> ) sample ball milled for 0.5 h (Q <sub>TR</sub> =36.4 kJ/g). (b) TG and DSC curves and (c) the change in the partial pressure of oxygen during desorption of a (H <sub>2</sub> +B <sub>2</sub> H <sub>6</sub> ) gas mixture. Heating rate 5°C/min.....	<b>42</b>
<b>Figure 23:</b> (a) Mass spectrometry (MS) gas desorption spectra for a (2NaBH <sub>4</sub> +MnCl <sub>2</sub> )+5 wt.% graphene sample ball milled for 0.5 h (Q <sub>TR</sub> =36.4 kJ/g). (b) TG and DSC curves during desorption of a (H <sub>2</sub> +B <sub>2</sub> H <sub>6</sub> ) gas mixture. Heating rate 5°C/min.....	<b>44</b>

<b>Figure 24:</b> (a) Mass spectrometry (MS) gas desorption spectra for a (2NaBH <sub>4</sub> +MnCl <sub>2</sub> ) +5wt.% LiNH <sub>2</sub> sample ball milled for 0.5 h (Q <sub>TR</sub> =36.4 kJ/g). (b) TG and DSC curves during desorption of a (H <sub>2</sub> +B <sub>2</sub> H <sub>6</sub> ) gas mixture. Heating rate 5°C/min.....	<b>46</b>
<b>Figure 25:</b> XRD patterns of the 0.5 h BM sample, solvent extracted at 42°C for 20 min (center) in comparison to the XRD patterns of the 0.5 h BM (2NaBH <sub>4</sub> +MnCl <sub>2</sub> ) (bottom) and (2LiBH <sub>4</sub> +MnCl <sub>2</sub> ) (top) samples.....	<b>48</b>
<b>Figure 26:</b> XRD patterns of the 1 h BM ball milled (2NaBH <sub>4</sub> +MnCl <sub>2</sub> )+5wt.% Ni sample, solvent extracted at 42°C for 25 min (top) in comparison to the XRD patterns of the same ball milled powder before extraction (bottom).....	<b>49</b>
<b>Figure 27:</b> Desorption curves for the (2NaBH <sub>4</sub> +MnCl <sub>2</sub> ) samples milled with a milling energy input Q <sub>TR</sub> =72.8 kJ/g for 1 h (a) after extraction, and (b) showing the effect of the extraction procedure, while (c) shows the Arrhenius plot of rate constant k with temperature for estimation of the apparent activation energy of hydrogen desorption: 1 h BM and extracted (Q <sub>TR</sub> =72.8 kJ/g): y= -90.15x+29.914; R <sup>2</sup> =0.9784.....	<b>51</b>
<b>Figure 28:</b> (a) Mass spectrometry (MS) gas desorption spectra for a (2NaBH <sub>4</sub> +MnCl <sub>2</sub> ) sample ball milled for 1 h (Q <sub>TR</sub> =72.8 kJ/g) and then extracted at 42°C using solvent filtration method. (b) TG and DSC curves during desorption of a (H <sub>2</sub> +B <sub>2</sub> H <sub>6</sub> ) gas mixture. Heating rate 5°C/min.....	<b>53</b>

## List of Tables

<b>Table 1:</b> Technical System Targets: Onboard Hydrogen Storage, selected data [11].....	<b>4</b>
<b>Table 2:</b> High capacity complex metal hydrides and their hydrogen storage properties [4].....	<b>5</b>
<b>Table 3:</b> Properties and chemical composition of ultrafine filamentary nickel used in this work (obtained from CNEM Corporation Canada).....	<b>10</b>
<b>Table 4:</b> Types of samples prepared for this work.....	<b>19</b>
<b>Table 5:</b> Experimental lattice spacings, $d_{(hkl)}$ , for crystalline, extracted $Mn(BH_4)_2$ obtained in this work from the 0.5 h and 1 h ball milled ( $2NaBH_4+MnCl_2$ ) mixtures, compared to $d_{(hkl)}$ values calculated from synchrotron radiation [16] and to the experimental ones obtained from SAEDP (selected area electron diffraction pattern) in [36].....	<b>50</b>

## **1. Introduction**

### ***1.1. Motivation***

In recent years, countries the world over have shown increasing interest in reducing their dependency on fossil fuels and transitioning to an economy based on clean renewable energy. This drive to shift to a clean energy future has been accelerated by the imminent threat of climate destabilization [1].

The concept of the Hydrogen Economy – a future economy based on hydrogen upon the exhaustion of coal as a source of power in the United Kingdom – was first proposed in 1923 by J.B.S. Haldane in his talk “Science and the Future” at Cambridge University [2]. Since then, the use of hydrogen as a potential future energy carrier has been widely suggested for a variety of industrial and commercial applications [3].

For this future to become reality, there are numerous issues that need to be addressed, chief among which is the safe and effective storage of hydrogen.

This issue is magnified for applications that require the power source to have a high degree of portability, such as vehicles (automobiles, ships and aircraft), small electronic devices and household appliances [4].

Therefore the motivation for the present work stems from the urgent need to find a viable hydrogen storage medium for mobile applications.

### ***1.2. Hydrogen Storage Methods for Mobile Applications***

One of the most widely used energy generation devices for the mobile applications listed above is the Proton Electrolyte Membrane Fuel Cell (PEMFC).

A PEMFC stack as used in vehicular or other mobile applications operates at 1.1-1.8 bar pressure and generates waste heat that increases coolant temperatures to 70-80°C.

### *1.2.1. High-pressure tanks*

Hydrogen is most commonly stored in steel high-pressure tanks that can withstand up to 300 bar cyclic pressure. More expensive and technologically complex custom composites reinforced with carbon-fibre tolerate up to 700 bar of pressure [5]. Even at these high pressures, these vessels store only about 4-5 wt. % H<sub>2</sub>, besides having low volumetric capacity ( $\approx 40 \text{ kg H}_2/\text{m}^3$ ) when taking into account the size of the storage container. Furthermore, there is imminent risk of hydrogen embrittlement [6] in steel vessels and high pressure poses a significant consumer safety risk.

### *1.2.2. Cryogenic storage*

This method of storage involves supercooling (to 20K) and liquefying hydrogen and storing it in an insulated pressure vessel [7]. This overcomes the disadvantage of low volumetric capacity of gaseous hydrogen and almost completely eliminates the safety risk associate with high-pressure cylinders. However, the disadvantages outweigh the benefits. Liquefying the hydrogen is cost and energy intensive as it requires a large amount of electricity. Also, the evaporation loss while fueling, and due to the heat and the environment, is catastrophic [8].

### *1.2.3. Solid State Hydrides*

Solid state hydrides overcome the drawbacks of both compressed and liquefied hydrogen storage. These metallic/intermetallic and complex chemical hydrides store hydrogen at low pressures and have high volumetric capacities. The hydrogen released from these

compounds is of very high (>99%) purity and can be used directly to power a Proton Exchange Membrane (PEM) fuel cell. The safest (and thus the most desirable) hydrides for storage release hydrogen through an endothermic reaction.

### ***1.3. US Department of Energy (DOE) Targets***

In 2012, The US Department of Energy (DoE) released a Multi-Year Research, Development and Demonstration Plan in which it published system targets to be met for on-board hydrogen storage by 2020, and also the ultimate desired target.

With regards to gravimetric capacity, it is important to note that *Table 1* lists the target *system* capacity and not the capacity of the material itself. Typically, the material gravimetric capacity required to meet the target is approximately twice that of the system capacity (~11 wt% for 2020).

Simple metal hydrides, of the type  $AB_x$ , typically have gravimetric capacities that are too low for practical applications. Among these, the only ones with high capacity –  $MgH_2$  and  $LiH$ , have very high desorption temperatures [9]

In a book addressing the challenges for hydrogen storage [10], the US Department of Energy (DoE) found that intermetallics, of the type  $A_xB_y$ , where both A and B are metals (such as Ni, Ti, La, Zn and Mn, among many others) were unsuitable for hydrogen storage for portable applications. Even though these compounds met the desorption pressure requirement of 1 atm as set by the DoE, they had very low gravimetric storage capacities in comparison to other solid state storage solutions.

<b>Technical System Targets: Onboard Hydrogen Storage for Light-Duty Fuel Cell Vehicles</b>			
<b>Storage Parameter</b>	<b>Units</b>	<b>2020</b>	<b>Ultimate</b>
System Gravimetric Capacity	wt%	5.5	7.5
System Volumetric Capacity	Kg H <sub>2</sub> /L	0.040	0.070
Storage System Cost	\$/kWh net	10	8
Fuel Cost	\$/gge at pump	2-4	2-4
Operating ambient temperature	°C	40/60	40/60
Min/max delivery temperature	°C	40/85	40/85
Onboard efficiency	%	90	90
System fill time (5 kg)	Min	3.3	2.5
Minimum flow rate	(g/s)/kW	0.02	0.02
Fuel Quality	% purity H <sub>2</sub>	99.97% dry basis	99.97% dry basis
Loss of usable H <sub>2</sub>	(g/h)/kg H <sub>2</sub>	0.05	0.05

*Table 1: Technical System Targets: Onboard Hydrogen Storage, selected data [11]*

As shown in *Table 2*, high capacity complex metal hydrides have desirable gravimetric storage capacities. However, most desorb their hydrogen at a far greater temperature than that required or tolerated by a PEM fuel cell.

<b>Metal-hydrogen system</b>	<b>Hydride</b>	<b>Theoretical maximum gravimetric H<sub>2</sub> capacity (wt%)</b>	<b>Theoretical reversible gravimetric capacity (wt%)</b>	<b>Approx. desorption temperature range (°C)</b>
Li-B-H	LiBH <sub>4</sub>	18.4	13.8	470
Mg-B-H	Mg(BH <sub>4</sub> ) <sub>2</sub>	14.9	11.2	300
Fe-B-H	Fe(BH <sub>4</sub> ) <sub>3</sub>	12.1	Unknown	Unknown
Ca-B-H	Ca(BH <sub>4</sub> ) <sub>2</sub>	11.6	Unknown	320
Na-B-H	NaBH <sub>4</sub>	10.6	10.6	400-600
Li-Al-H	LiAlH <sub>4</sub>	10.6	7.9	110-260
Al-H	AlH <sub>3</sub>	10.0	10.0	150
Mg-Al-H	Mg(AlH <sub>4</sub> ) <sub>2</sub>	9.3	7.0	110-160
Li-N-H	LiNH <sub>2</sub> (+LiH+TiCl <sub>3</sub> )	8.8	6.0	150-280
Zn-B-H	Zn(BH <sub>4</sub> ) <sub>2</sub>	8.5	8.5	85-140
Ca-Al-H	Ca(AlH <sub>4</sub> ) <sub>2</sub>	7.9	5.9	80-180
Mg-H	MgH <sub>2</sub>	7.6	7.6	300-400
Na-Al-H	NaAlH <sub>4</sub>	7.5	5.6	229-247
Mg-N-H	Mg(NH <sub>2</sub> ) <sub>2</sub> (+LiH)	7.2	7.0	140-250
Mg-Fe-H	Mg <sub>2</sub> FeH <sub>6</sub>	5.5	5.5	300-400
Na-N-H	NaNH <sub>2</sub>	5.3	Unknown	<200

*Table 2: High capacity complex metal hydrides and their hydrogen storage properties [4]*

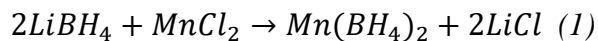
Of the compounds listed in *Table 2*, complex metal borohydrides from  $\text{LiBH}_4$  through  $\text{NaBH}_4$  have the highest theoretical maximum gravimetric hydrogen storage capacity. Some borohydrides with desorption temperatures closer to the operating temperature of a PEM fuel cell, like  $\text{ZnBH}_4$ , have shown to evolve diborane,  $\text{B}_2\text{H}_6$ , a foul smelling, highly toxic gas that destroys the PEM fuel cell membrane.

These materials also demonstrate a high rate of reversibility, albeit at high desorption temperatures and pressures. Lowering this temperature has been a long-standing challenge for researchers, and the DoE requirement that storage materials be reversible for the refueling to mimic present-day petrol and diesel fueling stations has been controversial.

#### ***1.4. Previous work***

This work is a part of a research program that is focused on studying irreversible hydride systems for relatively fast “on-demand” hydrogen generation either by mechanical or thermal energy input which could be synthesized in solid state by a process known as mechanochemical activation synthesis (MCAS).

This work is a continuation of previous studies by Varin et al. that reported a rapid release of hydrogen from a  $(2\text{LiBH}_4+\text{FeCl}_2)$  mixture under mechanical energy input through the formation/decomposition of amorphous/disordered  $\text{Fe}(\text{BH}_4)_2$  [12]. Similarly, Varin et al. and others have extensively studied a  $(2\text{LiBH}_4+\text{MnCl}_2)$  system that generates  $\text{H}_2$  under thermal energy input (thermolysis) at reasonably low temperatures through the formation and subsequent thermolysis of crystalline  $\text{Mn}(\text{BH}_4)_2$  [13, 14, 15, 16, 17, 18, 19]. So far, crystalline  $\text{Mn}(\text{BH}_4)_2$  has been synthesized by MCAS during ball milling as a result of a solid state metathesis reaction between  $2\text{LiBH}_4$  and  $\text{MnCl}_2$  [13, 14, 15, 16] according to



Mass spectrometry of the gas desorbed during thermolysis of crystalline  $\text{Mn}(\text{BH}_4)_2$  in the above reaction, combined with thermogravimetric analysis, showed the presence of varying quantities of diborane gas ( $\text{B}_2\text{H}_6$ ) mixed with hydrogen gas [17, 18]

However, very few studies have used another alkaline metal borohydride, such as  $\text{NaBH}_4$ , in the mechano-chemical synthesis of  $\text{Mn}(\text{BH}_4)_2$ . In general,  $\text{NaBH}_4$  is a much cheaper chemical compound than its counterpart,  $\text{LiBH}_4$ , which is an important economical factor. The most extensive study with  $\text{NaBH}_4$  was done by Severa et al. [20], which claimed that the manganese borohydride complexes synthesized by MCAS using both  $\text{NaBH}_4$  and  $\text{LiBH}_4$  as precursors were amorphous and could not be detected by X-ray diffraction.

Interestingly, studies prior to Severa et al. all support the formation of crystalline  $\text{Mn}(\text{BH}_4)_2$  when the  $\text{LiBH}_4$  precursor is used. Severa et al. [20] went further to claim that mechano-chemical activation synthesis of  $\text{LiBH}_4$  with  $\text{MnCl}_2$  produced amorphous  $\text{Mn}(\text{BH}_4)_2$  whereas changing the precursor to  $\text{NaBH}_4$  produced a different species: amorphous  $\text{Na}_2\text{Mn}(\text{BH}_4)_4$ .

Other studies such as Llamas-Jansa et al. [21] reported a formation of  $\text{Na}(\text{BH}_4)_{1-x}\text{Cl}_x$  solid solutions possessing cubic  $\text{NaCl}$ -type structure when a mixture of  $(3\text{NaBH}_4 + \text{MnCl}_2)$  was ball milled in a Fritsch Pulverisette planetary mono-mill.

Nakamori et al. [22, 23] reported that when  $\text{NaBH}_4$  was used in reaction (1) then only the  $\text{NaCl}$  peaks were present. This peculiar observation was interpreted by Nakamori et al. as evidence of the “disordering” (or, alternatively, amorphization) of the crystal structure of  $\text{Mn}(\text{BH}_4)_2$  in which there is no long-range order of the  $\text{Mn}^{2+}$  and  $(\text{BH}_4)^-$  units forming a proper crystalline structure, but a short-range order still exists.

Nakamori et al. [22, 23] concluded that reaction (1) with  $\text{LiBH}_4$  occurred more easily - producing crystalline  $\text{Mn}(\text{BH}_4)_2$  - than the same reaction with  $\text{NaBH}_4$ , owing to the similar ionic radii of  $\text{Li}^+$  (0.076 nm) and  $\text{Mn}^{2+}$  (0.067 nm) in the solid-solid cation exchange reaction (1) as compared to a larger ionic radius of  $\text{Na}^+$  (0.102 nm). Very recently, Guda et al. [24] used  $\text{NaBH}_4$  with  $\text{MnCl}_2$  to synthesize  $\text{Mn}(\text{BH}_4)_2$  by ball milling. They reported that the final product contained crystalline  $\text{Mn}(\text{BH}_4)_2$  and about 5 wt. % of  $\text{NaBH}_4$ . This result is rather surprising since they did not report the presence of  $\text{NaCl}$  which is a commonly observed by-product of the metathesis reaction between  $\text{NaBH}_4$  and  $\text{MnCl}_2$  (reaction (1) with  $\text{NaBH}_4$ ).

The effect of catalytic additives on the dehydrogenation kinetics of  $\text{Mn}(\text{BH}_4)_2$  has never been studied. The use of additives such as Reduced Graphene Oxide (RGO) and ultrafine filamentary nickel in small quantities is thought to attract hydrogen atoms to the surface of grains and facilitate the mechanism of formation of  $\text{H}_2$  molecules and their accelerated release at elevated temperatures.

### ***1.5. Statement of Objectives***

It is clear that there is still a disagreement about the nature of species produced by MCAS when the  $\text{NaBH}_4$  precursor/reactant is used in the mixture with  $\text{MnCl}_2$  in reaction (1). Therefore, the scientific objective of the present work is to investigate the microstructure of the  $(2\text{NaBH}_4+\text{MnCl}_2)$  mixture processed by ball milling and the effect of catalytic additives on its hydrogen generation behavior. Furthermore, for the first time, the results of the solvent extraction/filtration of  $\text{Mn}(\text{BH}_4)_2$  from a mixture with a  $\text{NaCl}$ -type salt will be presented and discussed. One of the most remarkable results in this work is the crystallization of likely amorphous  $\text{Mn}(\text{BH}_4)_2$  produced after MCAS during the subsequent filtration/extraction

process and the generation of ~7.5 wt. % of H<sub>2</sub> by this powder, which has never before been reported in literature.

## 2. Experimental Procedure

### 2.1. Sample Preparation

As received sodium borohydride,  $\text{NaBH}_4$ , of 98% purity, and manganese chloride,  $\text{MnCl}_2$ , of 99.99% purity, from Alfa Aesar Canada were mixed in a 2:1 molar ratio. A number of samples were prepared, some of which were mixed with 5 wt. % ultrafine filamentary nickel (Ni), 5 wt. % reduced graphene oxide (RGO) powder and 5 wt. % lithium amide ( $\text{LiNH}_2$ ).

The specialty Ni, grade N04 (as trademarked) was produced by a proprietary carbonyl method by CNEM Corporation Canada. Its properties are listed in *Table 3* below:

Apparent density ( $\text{g/cm}^3$ )	0.28
Fisher Sub-Sieve Size (FSSS) ( $\mu\text{m}$ )	0.85

Chemical composition	wt%
Ni	99
C	0.77
O	0.22
S	0.0015
Co	<0.001
Fe	<0.02

*Table 3: Properties and chemical composition of ultrafine filamentary nickel used in this work (obtained from CNEM Corporation Canada)*

The Few Layer Reduced Graphene Oxide platelets (flakes) (FL-RGO), referred to as “graphene” in the text, were obtained from Nanomaterials (<http://www.nanomaterials.pl>), Warsaw, Poland. The bulk density of graphene was  $2.1 \text{ g/cm}^3 (\pm 0.1 \text{ g/cm}^3)$ . The chemical

composition (by weight) of graphene is as follows:  $\geq 85\%$  carbon,  $\leq 10\%$  oxygen,  $\leq 1\%$  hydrogen,  $\leq 3\%$  nitrogen,  $\leq 0.1\%$  manganese sulfate and  $\leq 0.1\%$  ash.

As received lithium amide,  $\text{LiNH}_2$ , of 95% purity and density 1.178 g/ml, from Sigma Aldrich USA, was used as a catalytic additive in the experiment.

The powders were handled in a glove-box in which a moisture-absorbing Drierite granulated compound was used as a desiccant. On absorbing moisture, a colour change to purple was observed and the Drierite was replenished as needed. Before handling, the glove box was purged a few times with high purity argon gas (99.999% purity) in order to minimize any possible contamination by moisture or oxygen from air.

Each powder mixture was loaded separately into an air-tight milling vial with an O-ring and equipped with a pressure valve mounted on the lid. Four hardened steel balls were placed in the vial with the ball-to-powder weight ratio (R) of 132.

These mixtures were then ball milled in a Uni-Ball-Mill 5 magneto-mill apparatus purchased from A.O.C. Scientific Engineering Pty Ltd., Australia. The ball milling was carried out for 0.5, 1 and 5 h for each type of powder mixture in an ultra-high purity hydrogen gas atmosphere (purity 99.999%:  $\text{O}_2 < 2$  ppm;  $\text{H}_2\text{O} < 3$  ppm;  $\text{CO}_2 < 1$  ppm;  $\text{N}_2 < 6$  ppm;  $\text{CO} < 1$  ppm;  $\text{THC} < 1$  ppm) at  $\sim 450$  kPa pressure.

During milling, the strong impact mode (IMP68) was used, in which two magnets are positioned at 6 and 8 o' clock, at the distance of  $\sim 10$  and  $\sim 2$  mm, respectively, from the vial. The rotational speed of the milling vial was  $\sim 200$  rpm. The vial was continuously cooled by two strategically placed air fans during the milling process. The possible release of hydrogen

during ball milling was continuously monitored by the pressure increase observed in the milling vial, which was measured by a pressure gage (with an accuracy of  $\pm 0.1$  wt. %  $H_2$ ).

## ***2.2. Milling energy input and milling mode***

As mentioned in [4], the milling energy in the magneto-ball mill can be controlled by changing the angular positions of two strong NdFeB magnets and changing the number of hard steel balls (mass 65 g and 25 mm in diameter each) in a milling vial. The detailed semi-empirical method of calculating milling energy in the magneto-ball mill, Uni-Ball-Mill 5, and the quantity of milling energy input in (kJ) per unit mass  $\cdot$  hour (kJ/gh) can be found in [25].

For the milling mode IMP68-4B-R132, which was applied in the present work, the injected energy input per hour is  $Q_{TR132}=72.8$  kJ/gh [25, 26]. Then the total milling energy input,  $Q_{TR}$  (kJ/g), can be calculated for a duration of each milling event in hours (h) keeping all the other milling parameters fixed. This novel approach uses only one physical parameter for describing the conditions of ball milling, the quantity of injected energy (kJ/g), which makes it a universal milling parameter, directly related to the microstructural changes occurring during ball milling.

## ***2.3. Solvent extraction***

The figure below represents a schematic of the simple preliminary solvent extraction/filtration method performed. The ball milled powder mixtures ( $2NaBH_4+MnCl_2$ ,  $2NaBH_4+MnCl_2+5$  wt. % Ni and  $2NaBH_4+MnCl_2+5$  wt. % graphene) were each mixed with diethyl ether ( $Et_2O$ ) in the mass ratio of 1:4. This mixture was subsequently stirred at room temperature (RT) for 2 h at a rotational speed of 225 rpm in order to dissolve the newly formed  $Mn(BH_4)_2$  in the  $Et_2O$  solvent and separate it from NaCl.

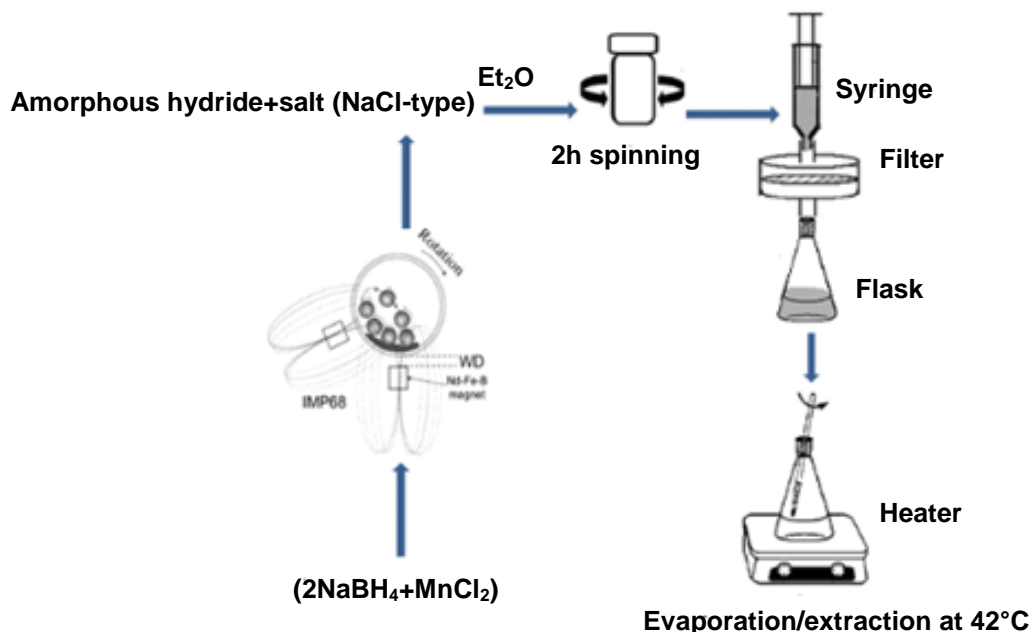


*Figure 1: Schematic of solvent extraction process used in this work for separation of  $\text{Mn}(\text{BH}_4)_2$  from the mixture with  $\text{NaCl}$*

The suspension after stirring was injected into a 60 ml syringe and filtered with a  $0.2 \mu\text{m}$  syringe filter. The filtering was done to collect  $\text{NaCl}$  at the filter and allow suspended  $\text{Mn}(\text{BH}_4)_2$  and in specific cases,  $\text{Ni}$  and graphene, to pass through the filter. In order to extract  $\text{Mn}(\text{BH}_4)_2$  from the suspension in  $\text{Et}_2\text{O}$ , an evaporation process of the suspension after filtering was carried out on a hot plate at a temperature of  $42^\circ\text{C}$  for 20 min, accompanied by simultaneous vigorous stirring at 1000 rpm to agitate the solution. A sample of the powder after evaporation was characterized by XRD and other techniques. The solvent extraction procedure was carried out entirely in the glove box that was purged and subsequently filled up with high purity argon gas (99.999% purity).

#### **2.4. Measurement of $\text{H}_2$ desorption**

The thermal gas desorption was evaluated by means of a second generation volumetric Sieverts-type apparatus custom-built by A.O.C. Scientific Engineering Pty Ltd., Australia.

This apparatus, built entirely of 316 austenitic stainless steel, allows loading a powder sample into a stainless steel reactor in a glove box under high purity argon and its subsequent transfer to the main unit in a sealed reactor without any exposure to the environment. Samples with a nearly constant masses of 30-40 mg were used in a desorption test. Before starting the desorption test, the inner tubing of the apparatus was evacuated and purged four times with ultra-high purity hydrogen.

With the inner tubing and reactor kept at 1 bar H<sub>2</sub>, the furnace of the apparatus was heated separately to the desired test temperature and the tightly sealed powder sample reactor was subsequently inserted inside. The powder sample in the reactor usually reaches the furnace temperature within ~400s in the temperature range of 100-200°C which is negligible compared to the time required to complete the desorption. Hence, the test can be considered as isothermal.

Desorption curves were corrected for the hydrogen gas expansion because of increase in temperature. The amount of desorbed hydrogen was calculated from the ideal gas law as described in detail in [4] and *Appendix A* and expressed in wt. % with respect to the *total* weight of powder sample. The calibrated accuracy of desorbed hydrogen capacity is about ±0.1 wt. % H<sub>2</sub> and that of temperature reading and stabilization ±0.1 °C. The apparent activation energy for volumetric hydrogen desorption was estimated using the registered dehydrogenation curves by applying a simple Arrhenius equation [4] following Sandrock et al. [27]:

$$k = k_0 e^{-\frac{E_A}{RT}} \quad (2)$$

In the equation, k is the slope of the linear portion of volumetric hydrogen desorption curves (rate of hydrogen desorption-wt. % H<sub>2</sub>/h) [28] recorded by the Sieverts-type apparatus, E<sub>A</sub> is the apparent activation energy in kJ/mol, R is the gas constant (8.314472 J/mol K), T is

absolute temperature (K) and  $k_0$  is a constant. The measured rates were plotted in the Arrhenius form as  $\ln k$  vs.  $1000/RT$ .

### ***2.5. X-ray Diffraction (XRD), SEM and FT-IR analysis***

The crystalline properties of the powders were characterized by a Bruker D8 X-ray diffractometer using a monochromated  $\text{CuK}\alpha_1$  radiation ( $\lambda = 0.15406$  nm) with an accelerating voltage of 40 kV and a current of 30 mA. The scan range was from  $2\theta=10$  to  $90^\circ$  and the rate was  $1.2^\circ/\text{min}$  with a step size of  $0.02^\circ$ . The powder sample was loaded in the glove box into a home-made brass holder with Cu/glass plates and a polymeric Kapton window transmittable to X-rays in the upper part of the sample holder.

The morphology of powders was studied using the LEO 1550 high resolution, field emission scanning electron microscope (FE-SEM) employing a secondary electron mode (SE) with the accelerating voltage of 10 kV. Powders were dispersed on a sticky carbon tape in a glove box filled with high purity argon and then transferred quickly to the SEM sample holder.

The Fourier transform infrared spectrometry (FT-IR) measurements were performed with a Nicolet 6700 apparatus at room temperature in the wavenumber range  $600\text{-}3000\text{ cm}^{-1}$  to examine the features of chemical bonding states of samples. The FT-IR apparatus was put in a glove bag and purged continuously with high purity (5N) nitrogen. The glove bag was opened and the glass vial containing a powder sample was inserted into a glove bag. After closing the glove bag the sample was dispersed onto the sample holder and inserted in the machine under nitrogen atmosphere. Subsequently, further measurements were carried out under the atmosphere of high purity (5N) nitrogen gas. The measurements were carried out in DRIFTS

mode. The raw data, with automatic background subtraction, were plotted. The resolution was  $4\text{ cm}^{-1}$  for all data and the units on the plots are Kubelka-Munk units.

## ***2.6. DSC and TGA analysis***

The differential scanning calorimetry (DSC) analysis was conducted simultaneously with the thermogravimetric analysis (TGA) on a Setaram Sensys Evo 3d analyzer (France). The analyzer was coupled with a quadrupole mass spectrometer Hiden Analytical (United Kingdom). Each powdered sample (~10-30 mg) was loaded into an alumina crucible of 100  $\mu\text{l}$  volume and covered with alumina powder almost to the top of the crucible to prevent the oxidation and hydrolysis during the quick transfer to the analyzer and also to avoid a volatile foaming and flowing out of the crucible if the powder sample melted. After loading to the analyzer, each sample was flushed with high purity helium gas (<10 ppm  $\text{O}_2$  and  $\text{H}_2\text{O}$ , BIP quality, Air Products) for 90 min and after that heating of sample was performed from 30 to  $520^\circ\text{C}$  with the rate of  $5^\circ\text{C}/\text{min}$ . Carrier helium gas flow was set to 28 ml/min. Hydrogen and diborane gas ( $\text{B}_2\text{H}_6$ ) level was measured with the use of mass spectrometer by analyzing the intensity of ions with the  $m/z=2$  ( $\text{H}_2$ ), 27 ( $\text{B}_2\text{H}_6$ ), 26 and 24 ratio (species that may form owing to the decomposition of  $\text{B}_2\text{H}_6$ ). For the purpose of graph plotting the measured pressure of escaping gases was normalized by the mass of the powder sample. Such a normalization was done because it allows a qualitative direct comparison of the peak intensities of various released gases observed on the mass spectrometry (MS) plots that will be discussed later in the present work. The mass normalizing was performed only to avoid misleading differences in signal intensities caused by different masses of the samples.

## ***2.7. Solvent extraction process***

The solvent extraction process described in *Chapter 2.3* and *Figure 1* had an average yield of 4.35%. Some changes were made in the process to enhance its yield. Most importantly, the mass ratio of powder mixture to diethyl ether was increased from 1:4 to 1:28, which means that for every 1g of powder, 28g of Et<sub>2</sub>O was added. First, 14g was added to the flask containing the powder, swirled (like wine in a glass) while closed with a rubber stopper until bubbling ceased. A slate grey precipitate and a pale yellow suspension was observed, which was transferred through the 60 ml syringe and 0.2 μm filter assembly into the second flask. Then the process was repeated (another 14g of Et<sub>2</sub>O was added to first flask and dissolved) while keeping the second flask closed with a rubber stopper. Then the content of the second flask was heated at 42°C for 25 min while stirring at 1000 rpm until the extract was obtained.

A sample of the powder obtained after evaporation was characterized by XRD and other techniques. A schematic of the improved process is shown in *Figure 2* below. The improved extraction process increased yield eleven-fold from 4.35% to 49.6%.

Previously, to obtain a sufficient yield for further investigation of the extracted sample, three batches of the ball milled starting powder mixture were required. After this minor process modification, a single batch was sufficient to provide enough yield for subsequent analyses.

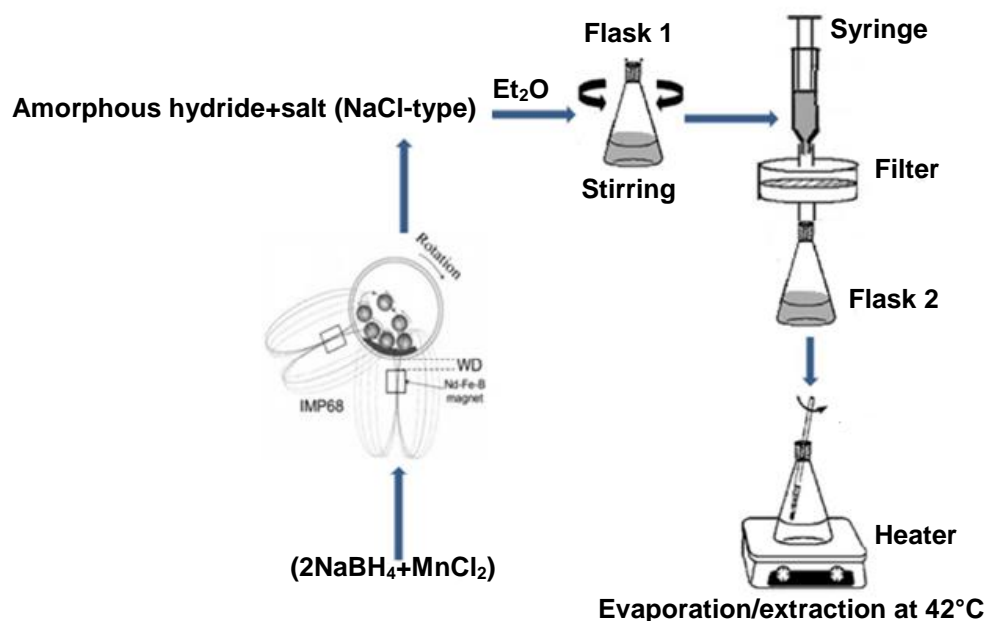


Figure 2: Schematic of the improved extraction process to remove NaCl from a mixture of  $\text{Mn}(\text{BH}_4)_2$  and NaCl

Table 4 below shows the different types of ball milled samples investigated in this work. As seen in the table, all solvent extraction was done with samples that were ball milled for 1 h, as this was the milling time that provided the most desirable desorption characteristics. This fact is discussed further in the next chapter of this work.

Milling time »	0.5 h	1 h	5 h
<b>Sample</b>			
2NaBH <sub>4</sub> + MnCl <sub>2</sub>	•	•	•
2NaBH <sub>4</sub> + MnCl <sub>2</sub> + 5 wt. % graphene	•		
2NaBH <sub>4</sub> + MnCl <sub>2</sub> + 5 wt. % Ni	•	•	
2NaBH <sub>4</sub> + MnCl <sub>2</sub> + 5 wt. % LiNH <sub>2</sub>	•		
2NaBH <sub>4</sub> + MnCl <sub>2</sub> (extracted)		•	
2NaBH <sub>4</sub> + MnCl <sub>2</sub> + 5 wt. % Ni (extracted)		•	

*Table 4: Types of samples prepared for this work*

### 3. Results and discussion

#### 3.1. Characterization of morphology and microstructure of the ball-milled samples

During the ball milling of the  $2\text{NaBH}_4 + \text{MnCl}_2$  powder mixture, the pressure in the milling vial was continuously monitored by a pressure gage. For all three milling times (0.5 h, 1 h and 5 h), no gas release was detected. This means that the mixture with  $\text{NaBH}_4$  precursor is more stable during ball milling than its  $\text{LiBH}_4$  counterpart, which in previous studies by Varin et al. desorbed about 0.2 and 0.3 wt. %  $\text{H}_2$  during milling for 0.5 and 1 h [18], respectively.

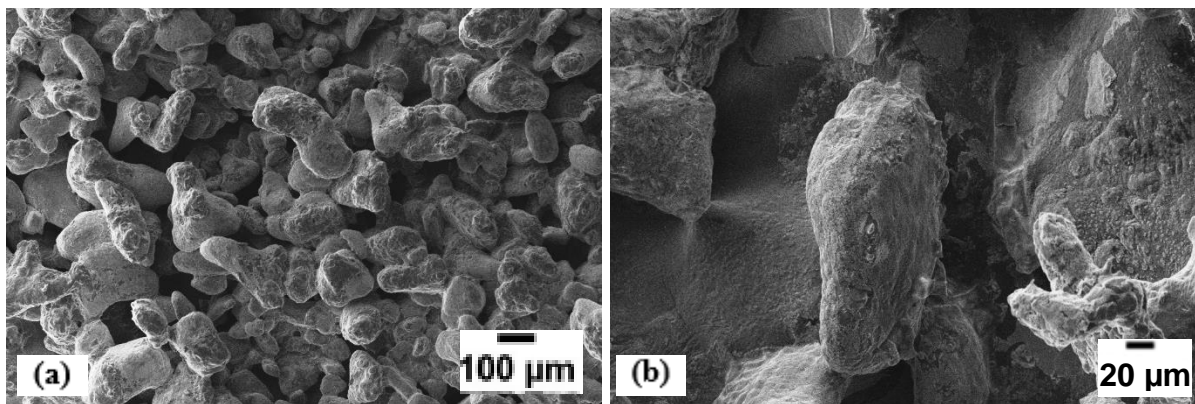


*Figure 3: SEM micrographs of as received  $\text{NaBH}_4$  (a) lower magnification and (b) higher magnification*

*Figure 3 (a) and (b)* show scanning electron micrograph images of the as-received  $\text{NaBH}_4$  reactant. The crystals are regularly shaped and rounded and are white in colour. Their dimensions are quite coarse, ranging from roughly 100 to 500  $\mu\text{m}$ . In contrast, the morphology of the as received  $\text{MnCl}_2$  reactant (*Figure 4 (a) and (b)*) appears to be globular, resembling agglomerates of fibrous, thinner particles.  $\text{MnCl}_2$  is pink in colour.

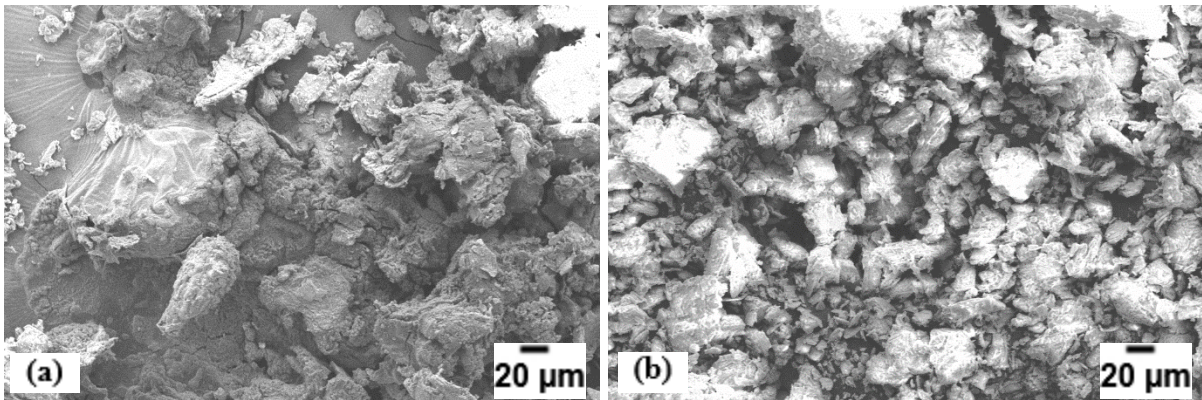


*Figure 4: SEM micrographs of as received  $\text{MnCl}_2$  [20] (a) lower magnification and (b) higher magnification*

*Figure 5 (a) and (b) show the evolution of morphology of the  $(2\text{NaBH}_4+\text{MnCl}_2)$  mixture after 0.5 h ( $Q_{\text{TR}}=36.4$  kJ/g), 1 h ( $Q_{\text{TR}}=72.8$  kJ/g) and 5 h ( $Q_{\text{TR}}=364$  kJ/g) of milling duration in the magneto-mill, Uni-Ball-Mill.*

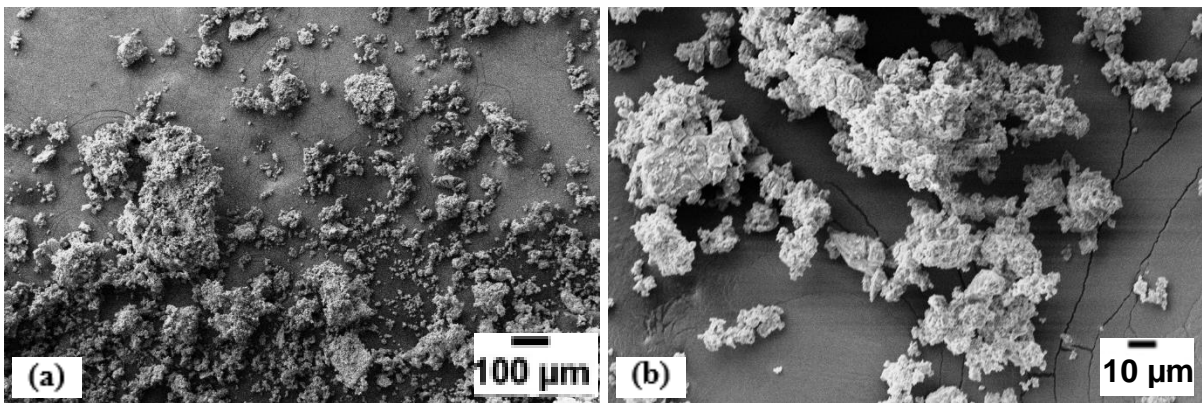


*Figure 5: SEM micrographs of  $2\text{NaBH}_4+\text{MnCl}_2$  0.5 h BM ( $Q_{\text{TR}}=36.4$  kJ/g) (a) lower magnification and (b) higher magnification*

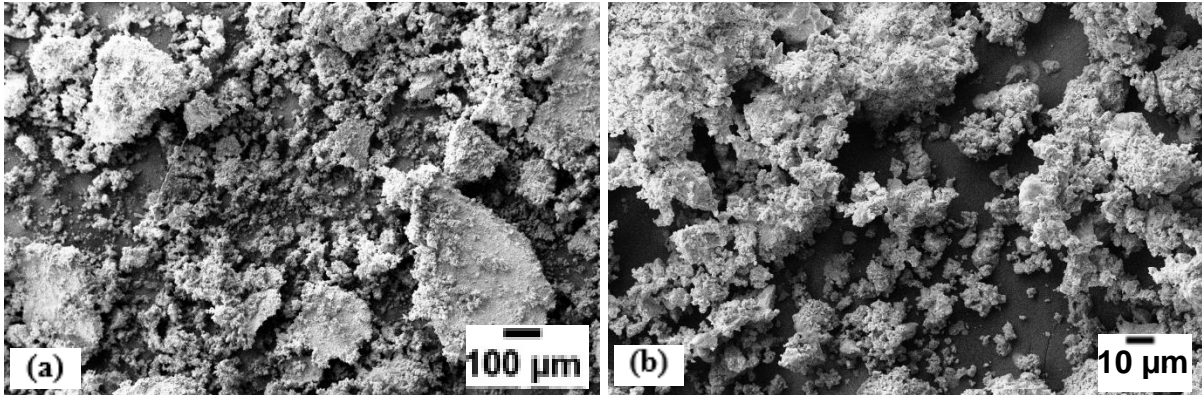


*Figure 6: SEM micrographs of NaBH<sub>4</sub>+MnCl<sub>2</sub> 5 h BM ( $Q_{TR}=364$  kJ/g) (a) lower magnification and (b) higher magnification*

The energy input injected into the powder mixtures after 0.5 h ball milling is, in general, rather small ( $Q_{TR}=36.4$  kJ/g). By comparison with the as-received morphology of both reactants, it is clear that a very substantial powder particle refinement was achieved after injecting a relatively small milling energy input. However, some large, agglomerated granules of powder are also observed.

The particulate morphology after 1 h ball milling ( $Q_{TR}=72.8$  kJ/g) was very similar to that in *Figure 5* and is not shown here. It will be argued later that the morphology/microstructure of the (2NaBH<sub>4</sub>+MnCl<sub>2</sub>) mixture, obtained after 1 h of milling, exhibited the optimal dehydrogenation properties.

In *Figure 6*, it can be seen that after injecting a ten-fold larger milling energy input ( $Q_{TR}=364$  kJ/g) for 5 h than that after 0.5 h of milling, any further particle refinement is not observed and instead, some agglomerated granules seem to be converted into thin “slabs” of heavily compacted powder. It will be shown later that this type of microstructure has some detrimental effect on the dehydrogenation properties of the (2NaBH<sub>4</sub>+MnCl<sub>2</sub>) mixture milled for 5 h.

The color of the milled powder turned to a pale brown, which is substantially different than the colors of both initial reactants mentioned above. That color change clearly indicates that a chemical reaction must have occurred upon ball milling.

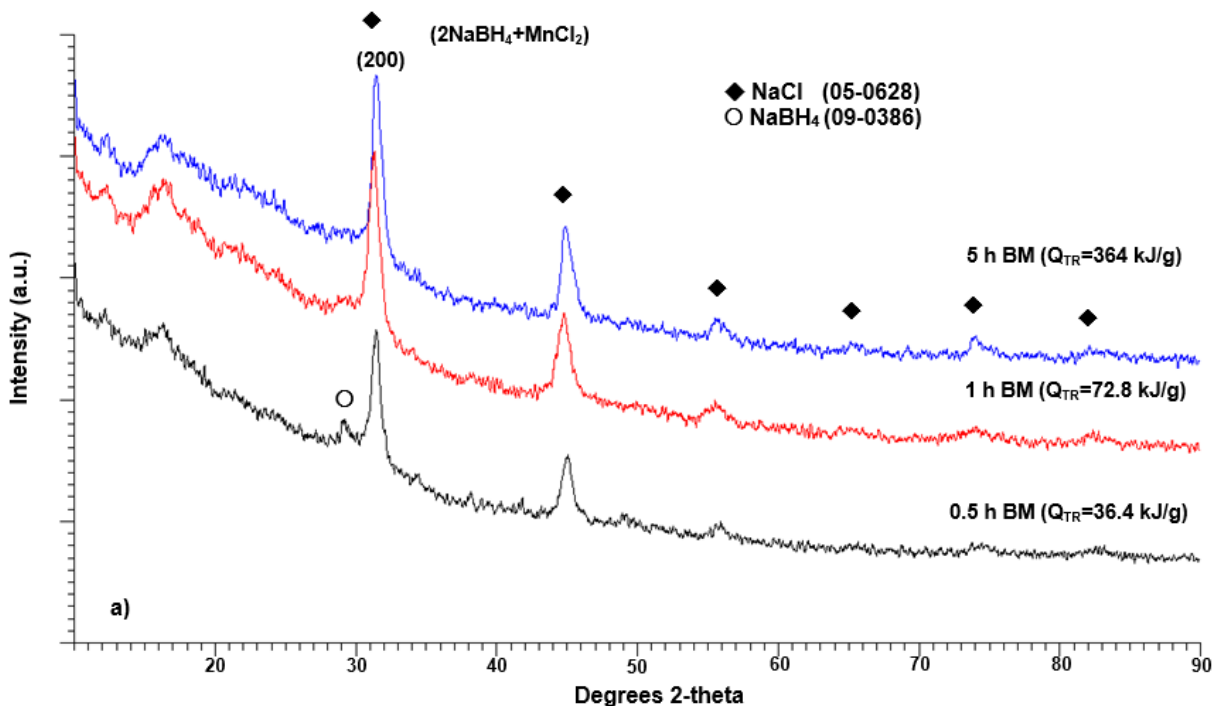


Figure 7: XRD patterns for the  $(2\text{NaBH}_4+\text{MnCl}_2)$  mixture ball milled for 0.5 h ( $Q_{\text{TR}}=36.4$  kJ/g), 1 h ( $Q_{\text{TR}}=72.8$  kJ/g) and 5 h ( $Q_{\text{TR}}=364$  kJ/g).

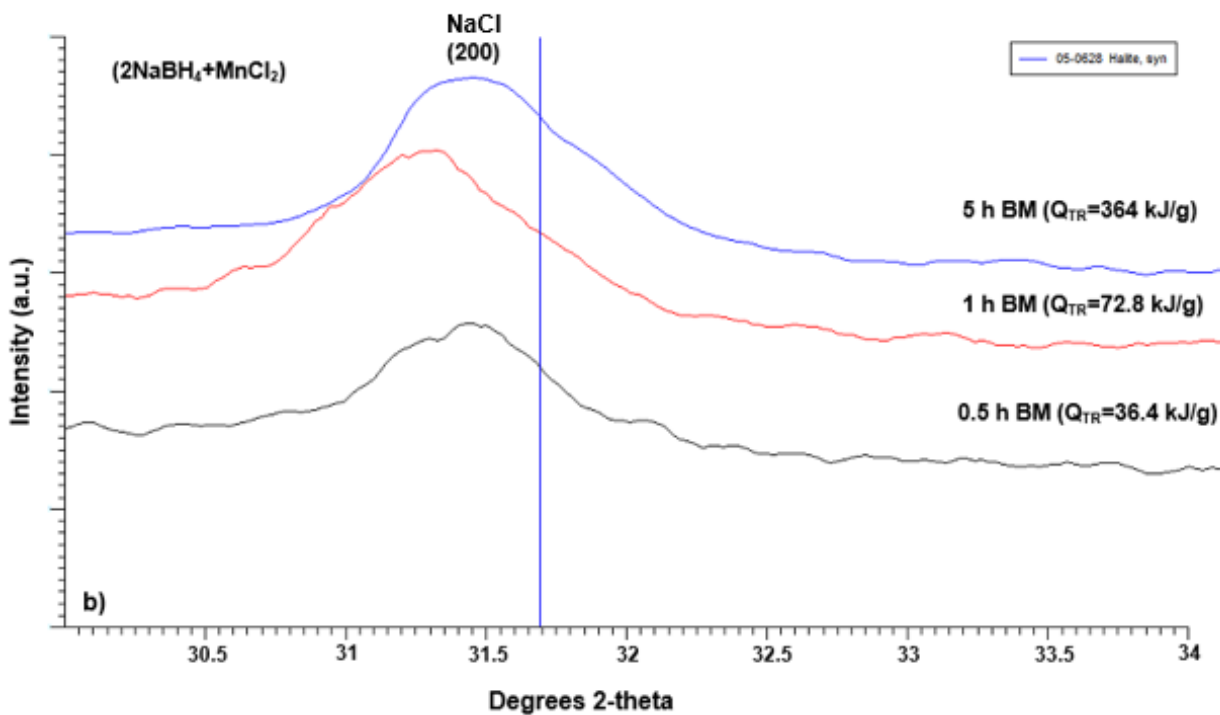


Figure 8: Enlargement of the (200) NaCl peak (100% intensity) in comparison to the (200) standard diffraction line from the ICDD PDF#(05-0628).

Figure 7 shows the XRD patterns of the  $(2\text{NaBH}_4+\text{MnCl}_2)$  mixture ball milled for 0.5, 1 and 5 h with increasing milling energy input from  $Q_{\text{TR}}=36.4$  to 364 kJ/g. The most striking feature of all XRD patterns is the presence of the diffraction peaks whose  $2\theta$  diffraction angles are close to the standard positions of the NaCl salt (ICDD PDF#(05-0628)) and nearly complete absence of any other peaks except a very weak (200) peak belonging to  $\text{NaBH}_4$  in the mixture after 0.5 h and, to a lesser extent, after 1 h ball milling, making it apparent that a small quantity of retained  $\text{NaBH}_4$  is still present in the structure. No peaks of crystalline  $\text{Mn}(\text{BH}_4)_2$  ( $\text{c-Mn}(\text{BH}_4)_2$ ) are observed. In the case of previous studies with  $\text{LiBH}_4$  as precursor, these were usually well visible in [3, 12, 13, 14] and other studies. This clearly shows that that  $\text{NaBH}_4$  in the initial mixture must have reacted with  $\text{MnCl}_2$  forming a NaCl-type salt as a by-product and a hydride that does not exhibit the XRD Bragg peaks. This particular observation of the lack of the crystalline  $\text{Mn}(\text{BH}_4)_2$  diffraction peaks is in an excellent agreement with the earlier XRD

results reported by Nakamori et al. [22, 23] where they reported formation of disordered/amorphous  $\text{Mn}(\text{BH}_4)_2$ .

*Figure 8* shows the enlargement of the (200) NaCl peak (100% intensity) in comparison to the (200) standard diffraction line from the ICDD PDF#(05-0628). The peak is heavily broadened indicating the formation of nano-grains within the NaCl particles or, alternatively, formation of nano-sized, monocrystalline NaCl particles as a fraction of the total particle population. Furthermore, the peak maximum is always shifted from the (200) NaCl standard diffraction position given by the ICDD PDF#(05-0628) file. This peculiar shift is not an artifact but has been observed after MCAS of every  $(2\text{NaBH}_4+\text{MnCl}_2)$  mixture. As mentioned earlier, Llamas-Jansa et al. [21] reported a formation of the  $\text{Na}(\text{BH}_4)_{1-x}\text{Cl}_x$  solid solution possessing a cubic NaCl-type structure.

Following Llamas-Jansa et al. [21], it is possible that the NaCl peaks shift in *Figure 8* is owing to the formation of a solid solution where either the  $\text{Cl}^-$  anions are being substituted by the  $(\text{BH}_4)^-$  anions or vice versa leading to the formation of the solid solution  $\text{Na}(\text{Cl})_x(\text{BH}_4)_{(1-x)}$  possessing a cubic NaCl-type crystalline structure.

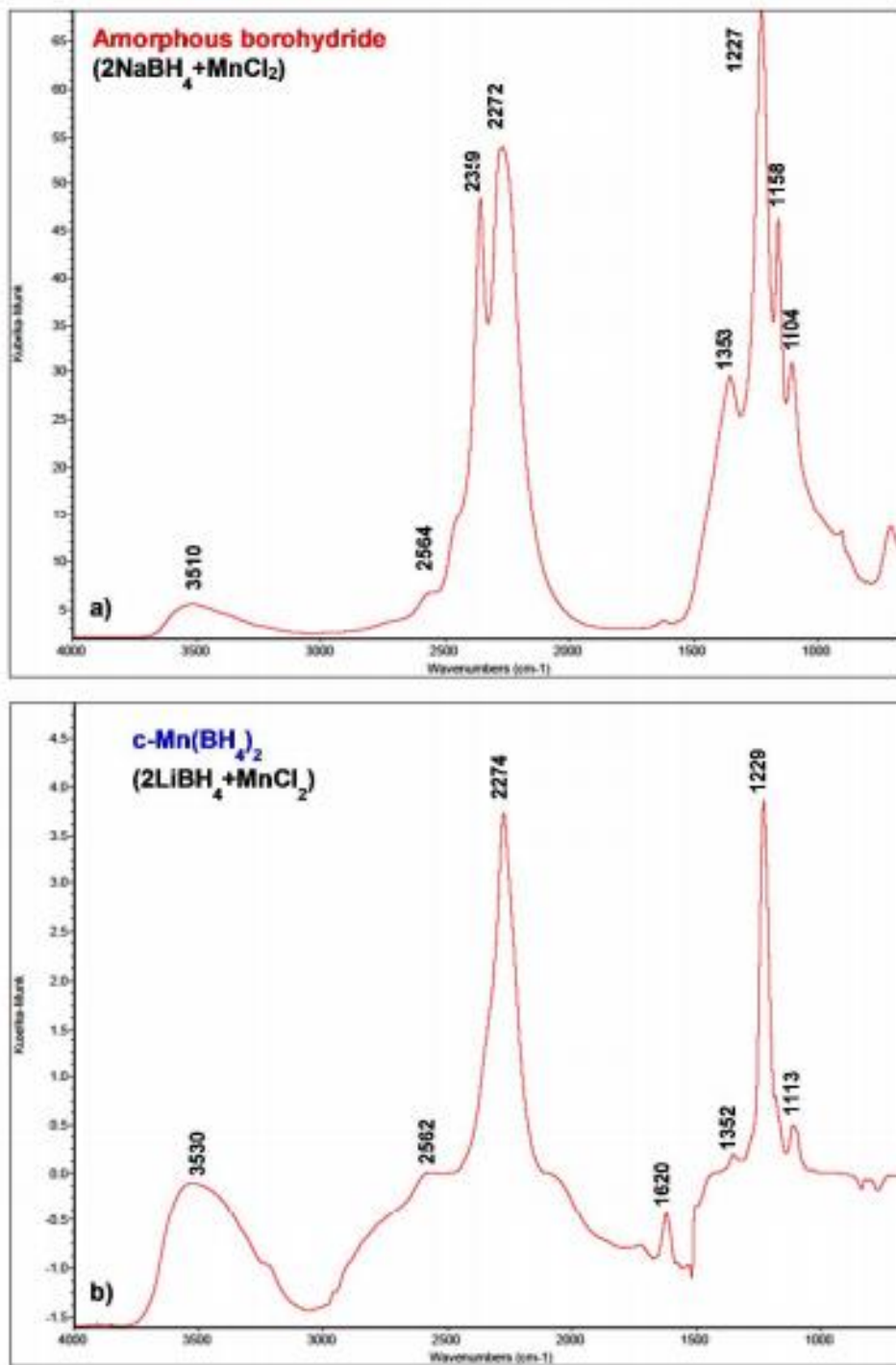


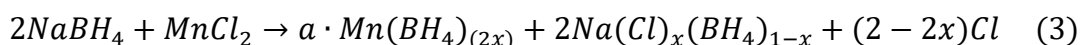
Figure 9: (a) FT-IR spectrum for a (2NaBH<sub>4</sub>+MnCl<sub>2</sub>) sample ball milled for 5 h ( $Q_{TR}=364$  kJ/g). (b) Reference FT-IR spectrum for a (2LiBH<sub>4</sub>+MnCl<sub>2</sub>) sample ball milled for 2 h ( $Q_{TR}=145.6$  kJ/g) containing a synthesized, crystalline Mn(BH<sub>4</sub>)<sub>2</sub> hydride (adopted from [16, 18])

Further support for the presence of a-Mn(BH<sub>4</sub>)<sub>2</sub> after BM is provided by the FT-IR spectrum in *Figure 9a* for the ball milled (2NaBH<sub>4</sub>+MnCl<sub>2</sub>) mixture compared to a reference spectrum for a ball milled (2LiBH<sub>4</sub>+MnCl<sub>2</sub>) mixture in *Figure 9b*. The latter was obtained for a crystalline, c-Mn(BH<sub>4</sub>)<sub>2</sub> hydride, synthesized by MCAS [18]. It is clearly seen that both spectra are very similar. The spectrum for a-Mn(BH<sub>4</sub>)<sub>2</sub>, synthesized by MCAS in the (2NaBH<sub>4</sub>+MnCl<sub>2</sub>) mixture (*Figure 9a*), exhibits two principal peaks, one within the 1000-1500 cm<sup>-1</sup> range, centered at the 1227 cm<sup>-1</sup> maximum and the other within the 2000-2500 cm<sup>-1</sup> wavelength range, centered at 2272 cm<sup>-1</sup>, respectively. Very similar two principal peaks are observed in the FT-IR spectrum for c-Mn(BH<sub>4</sub>)<sub>2</sub> synthesized by MCAS in the (2LiBH<sub>4</sub>+MnCl<sub>2</sub>) mixture (*Figure 9b*). The first peak within the 1000-1500 cm<sup>-1</sup> wavelength range is centered at 1229 cm<sup>-1</sup> and the second one at the 2000-2500 cm<sup>-1</sup> wavelength range, is centered at 2274 cm<sup>-1</sup>. The striking similarity between the full IR spectra for a-Mn(BH<sub>4</sub>)<sub>2</sub> and crystalline, c-Mn(BH<sub>4</sub>)<sub>2</sub>, is quite convincing evidence that the a-Mn(BH<sub>4</sub>)<sub>2</sub> hydride has, indeed, been synthesized in the ball milled (2NaBH<sub>4</sub>+MnCl<sub>2</sub>) mixture. The FT-IR spectrum in *Figure 9a* is also very similar to the crystalline Mn(BH<sub>4</sub>)<sub>2</sub> spectrum available in the FT-IR data bases [29, 30]. Furthermore, Choudhury et al. [19] reported for Mn(BH<sub>4</sub>)<sub>2</sub> obtained by MCAS from the (2NaBH<sub>4</sub>+MnCl<sub>2</sub>) mixture, the presence of broad peaks within the 1126-1213 and 2224-2372 cm<sup>-1</sup> wavelength range, found in the solid state FT-IR spectrum and confirmed by the density functional theory (DFT) modeling, which corresponded to the B-H bending deformation and stretching modes, respectively. The reported FT-IR wavelength ranges in [19] are in excellent agreement with those observed in *Figure 9a*.

The smaller peaks visible on the principal peak for a-Mn(BH<sub>4</sub>)<sub>2</sub> in *Figure 9a* at 1104 and 1158 cm<sup>-1</sup> can be assigned, more specifically, to the BH<sub>2</sub> or bridge deformation

(bidentate/tridentate/ionic structure) [28]. A small peak appearing at the  $1353\text{ cm}^{-1}$  wavelength could be assigned to either the B-H bridge stretching (bidentate structure) [28] or the B-H bridging bending modes [31]. The peaks at  $1620$  and  $3500\text{ cm}^{-1}$  could be attributed to a  $\text{H}_2\text{O}$  bending mode and the O-H stretching modes, respectively [31]. These peaks can be likely a result of some short-term air exposure during loading a sample into a holder for the FT-IR apparatus, as described in *Chapter 2*.

Therefore, it is finally postulated here that the mechano-chemically activated metathesis reaction occurs as follows:



In the above equation,  $0 < x \leq 1$  and  $a\text{-Mn}(\text{BH}_4)_{(2x)}$  is an amorphous manganese borohydride mechano-chemically synthesized during ball milling. For  $x=1$ , reaction (3) is reduced to reaction (1) for a  $\text{NaBH}_4$  reactant. Owing to the presence of heavier Na, the theoretical  $\text{H}_2$  capacity of reaction (3) for the  $\text{NaBH}_4$  reactant is about 4.0 wt. % at  $x=1$  which is 0.76 wt. %  $\text{H}_2$  lower than that of reaction (1) for the  $\text{LiBH}_4$  precursor [18]. For  $x < 1$  Eq. (3) would require the amorphous manganese borohydride,  $a\text{-Mn}(\text{BH}_4)_{(2x)}$  to be non-stoichiometric. It is hypothesized that this non-stoichiometry could prevent attaining a stoichiometric, crystalline structure during formation of the borohydride by mechano-chemical activation synthesis during ball milling. This aspect requires further in-depth study, possibly by neutron diffraction (PND) techniques as those reported by Llamas-Jansa et al. [21] in order to find out the value of  $x$  in equation (3). In addition, since  $x$  Eq. (3) is expected to be close to 1, the Cl quantity would be miniscule.

### 3.2. Characterization of morphology and microstructure of ball-milled samples with catalytic additives

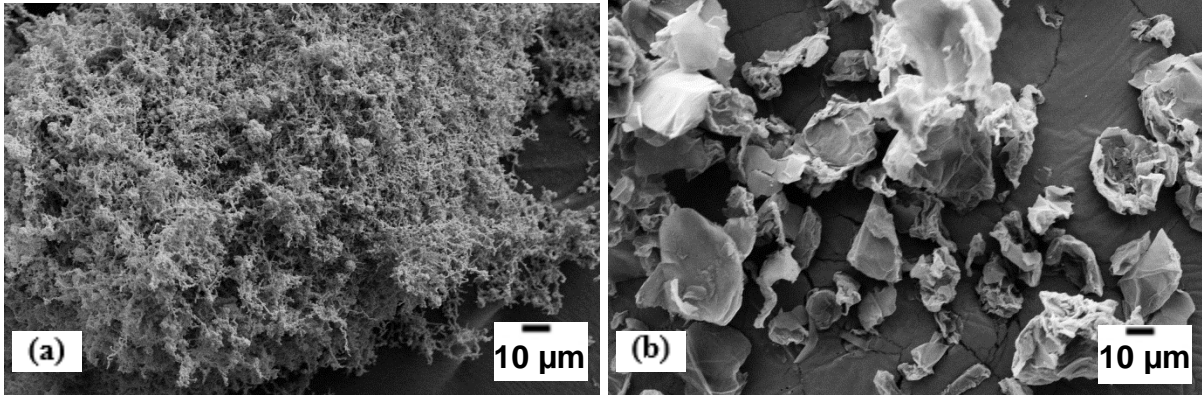
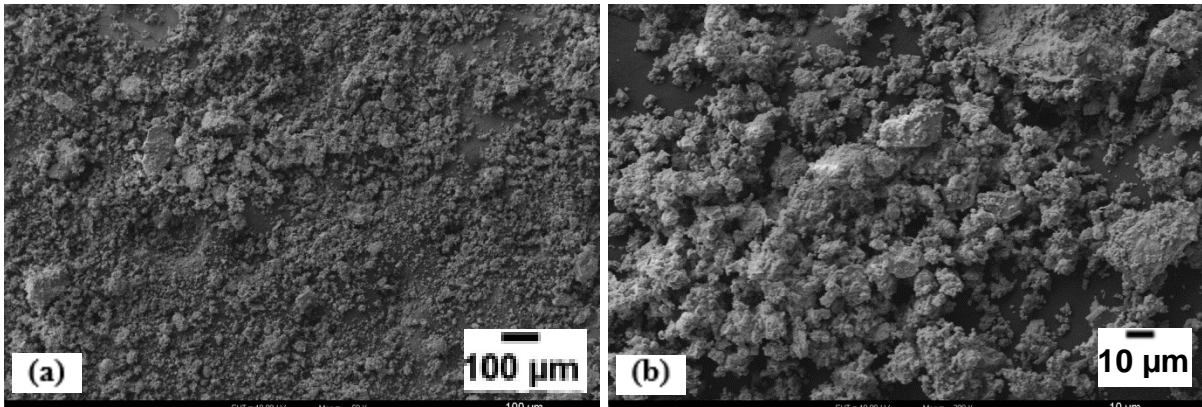


Figure 10: SEM images of (a) Filamentary nickel N04 and (b) graphene

In *Figure 10(a)*, the filamentary nature of the ultrafine nickel N04 powder is clearly visible. *Figure 10(b)* shows that the graphene used was fairly regular in size (15-20  $\mu\text{m}$ ) and was in the form of thin flakes.

*Figure 11* and *Figure 12* show that the powder morphology after milling with catalytic additives graphene and ultrafine filamentary nickel is strikingly similar. Both micrographs at high magnification (300-350x) demonstrate the presence of irregularly shaped but regularly sized chips with general clustering and occasional agglomeration. Also, in both cases, in comparison with the powder milled without additives (*Figure 5*), at a lower magnification (50x) it can be seen that greater particle refinement has been obtained. This corresponded with improved dehydrogenation properties as demonstrated later in this chapter.

Intermixing of graphene/nickel during milling turned the colour of the powder in both cases dark grey as compared to pale grey before milling.



*Figure 11: SEM micrographs of  $(2\text{NaBH}_4+\text{MnCl}_2)+5$  wt. % graphene 0.5 h BM ( $Q_{\text{TR}}=36.4$  kJ/g) (a) lower magnification (b) higher magnification*

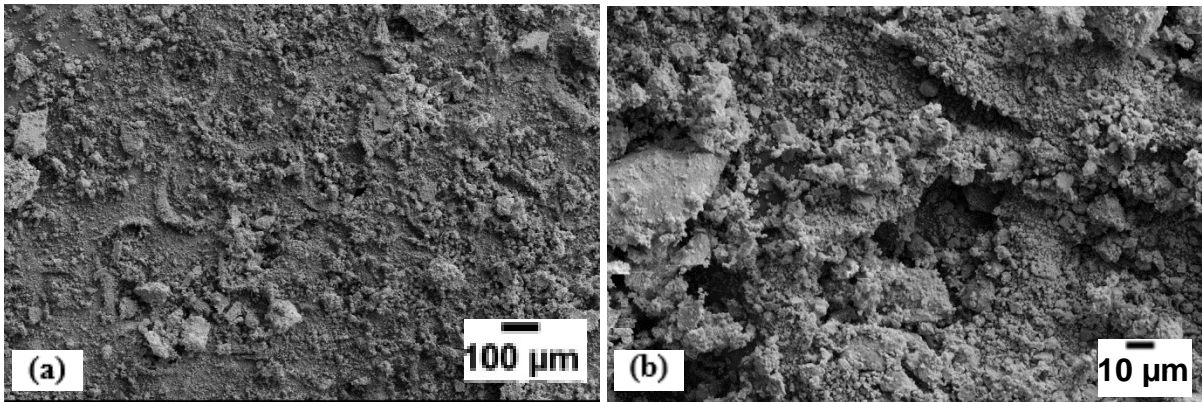


*Figure 12: SEM micrographs of  $(2\text{NaBH}_4+\text{MnCl}_2)+5$  wt. % Ni 0.5 h BM ( $Q_{\text{TR}}=36.4$  kJ/g) (a) lower magnification (b) higher magnification*

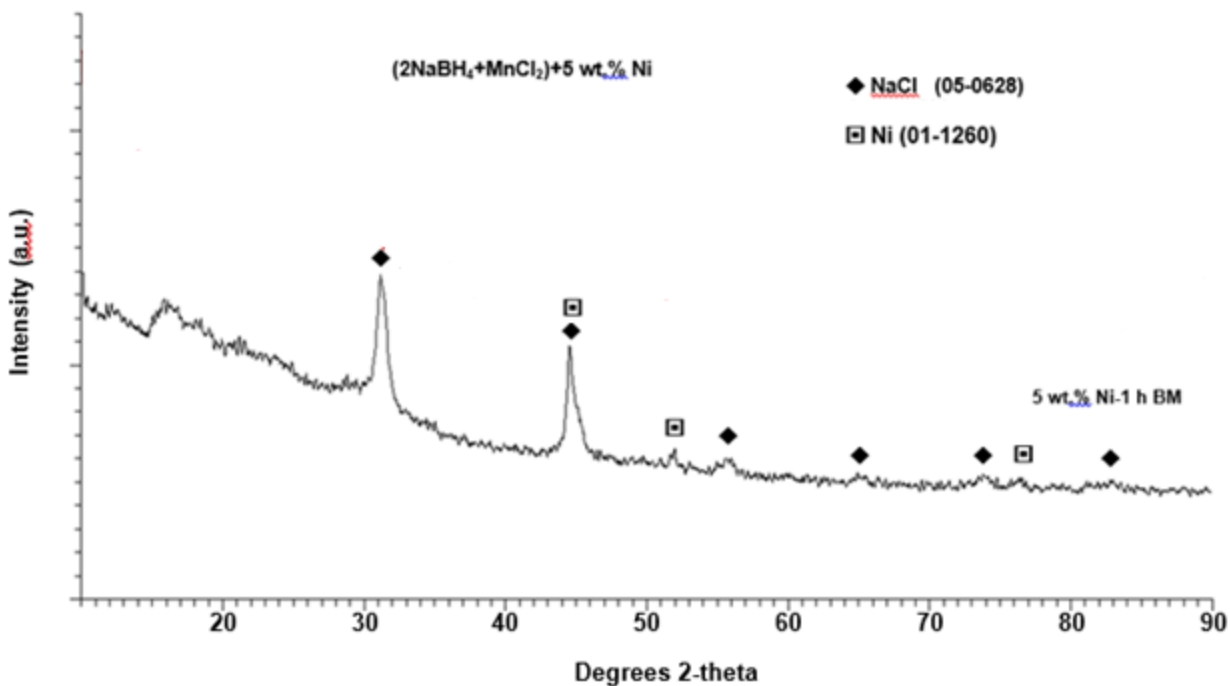


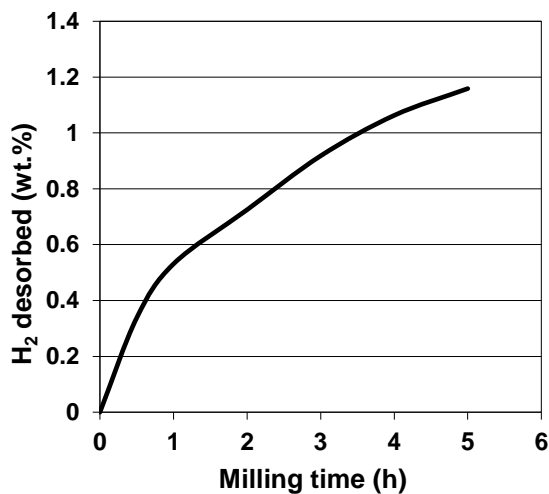
Figure 13: XRD patterns for the  $(2\text{NaBH}_4+\text{MnCl}_2)+5\text{wt. \% Ni}$  mixture ball milled for 1 h ( $Q_{\text{TR}}=72.8 \text{ kJ/g}$ )

Figure 13 shows the XRD patterns of the  $(2\text{NaBH}_4+\text{MnCl}_2)+5\text{wt. \% Ni}$  mixture ball milled for 1 h with milling energy input  $Q_{\text{TR}}=72.8 \text{ kJ/g}$ . As in Figure 7, the NaCl diffraction peaks'  $2\theta$  angles match closely with the standard positions of the NaCl salt (ICDD PDF#(05-0628)) and no peaks of crystalline  $\text{Mn}(\text{BH}_4)_2$  (c- $\text{Mn}(\text{BH}_4)_2$ ) are observed. There is no observable  $\text{NaBH}_4$  peak, which shows that it has been completely eliminated in the structure. One overlapping and two independent peaks attributable to Ni are also observed.

### 3.3. Characterization of morphology and microstructure of ball-milled samples doped with 5 wt. % $\text{LiNH}_2$

During the ball milling of the  $(2\text{NaBH}_4+\text{MnCl}_2)+5 \text{ wt. \% LiNH}_2$  powder mixture, the pressure in the milling vial was continuously monitored by a pressure gage. Figure 14 shows the weight percentage of  $\text{H}_2$  lost when it was released by the powder mixture during ball milling from 0 – 5 h.

More than 0.5 wt. % of H<sub>2</sub> is lost during the first hour of milling. This loss gradually slows as the milling time increases. After 5 hours, nearly 1.2 wt. % of H<sub>2</sub> is lost from the powder mixture. Due to the significant loss of H<sub>2</sub> observed with increasing milling time, the hydrogen desorption performance was assessed for the (2NaBH<sub>4</sub>+MnCl<sub>2</sub>)+5wt. % LiNH<sub>2</sub> mixture ball milled for 0.5 h only. However, experimental desorption at 100°C was carried out for the powder mixture milled for 1 h to understand the role and behaviour of LiNH<sub>2</sub> in the system.



*Figure 14: Amount of H<sub>2</sub> lost during ball milling of (2NaBH<sub>4</sub>+MnCl<sub>2</sub>)+5wt. % LiNH<sub>2</sub> mixture for 0 – 5 h*

The morphology for the above powder is shown in *Figure 15* below. There is a stark contrast in the nature of the powder compared to *Figure 11a-b* and *Figure 12a-b*. It demonstrates the ability of the LiNH<sub>2</sub> additive to achieve a much greater level of particle refinement than graphene or Ni. The particles are of the range 1-5 μm and are clustered to some degree to form irregular chunks. The colour of the mixture after milling was light brown and matched closely with the off-white colour of as-received LiNH<sub>2</sub>.



*Figure 15: SEM micrograph of (2NaBH<sub>4</sub>+MnCl<sub>2</sub>)+5wt. % LiNH<sub>2</sub> 0.5 h BM ( $Q_{TR}=36.4$  kJ/g).*

*Figure 16* shows the XRD patterns of the (2NaBH<sub>4</sub>+MnCl<sub>2</sub>)+5wt. % LiNH<sub>2</sub> powder mixture before milling and after it was ball milled for 0.5 h and 1 h with milling energy input  $Q_{TR}=36.4$  kJ/g  $Q_{TR}=72.8$  kJ/g respectively. It also shows the XRD of the 1 h ball milled powder desorbed at 100°C.

The XRD pattern of the powder mixture before ball milling indicates clear presence of the reactants: NaBH<sub>4</sub>, MnCl<sub>2</sub> and LiNH<sub>2</sub>. After milling for 0.5 h, broad peaks of NaCl are observed that indicates a substitution reaction has taken place resulting in nano-grain formation. The short NaCl peaks, paired with the complete absence of NaBH<sub>4</sub> or the new hydride suggests that a-Mn(BH<sub>4</sub>)<sub>2</sub> and/or a complex solid solution may have been formed. A longer milling time of 1 h results in distinct NaCl peaks and the continued absence of Mn(BH<sub>4</sub>)<sub>2</sub> peaks, which is consistent with the pattern observed in *Figure 7*.

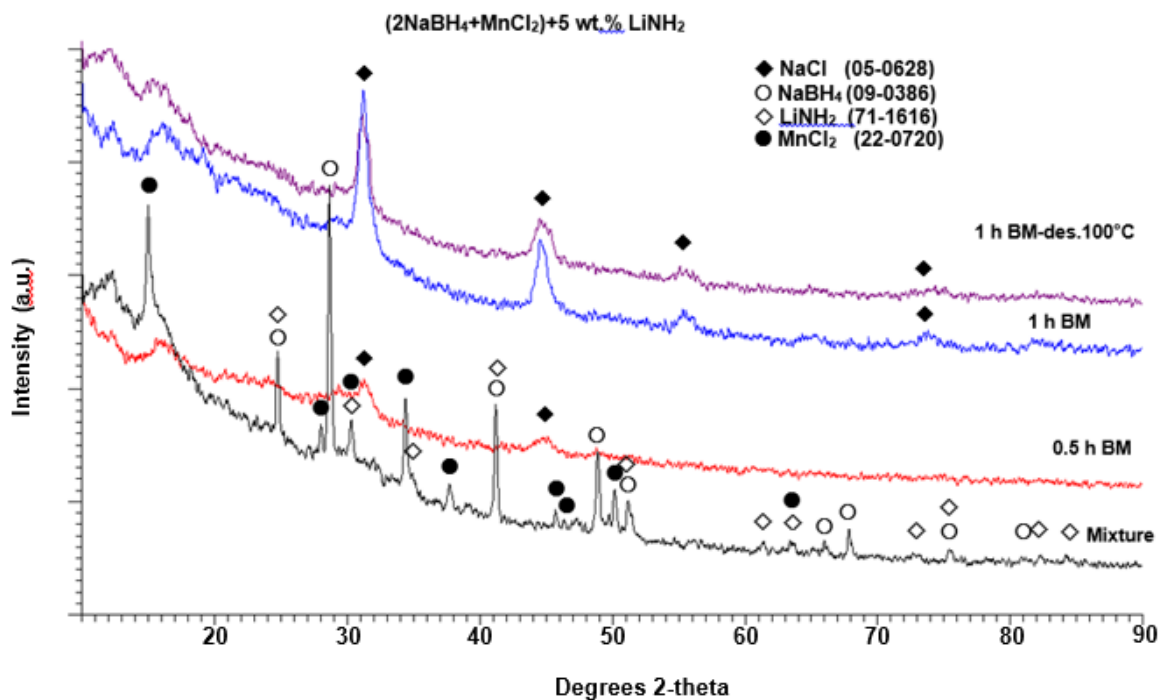


Figure 16: XRD patterns for the  $(2\text{NaBH}_4 + \text{MnCl}_2) + 5 \text{ wt. \% LiNH}_2$  mixture before ball milling, after being ball milled for 0.5 h ( $Q_{\text{TR}} = 36.4 \text{ kJ/g}$ ) and 1 h ( $Q_{\text{TR}} = 72.8 \text{ kJ/g}$ ), and after desorption at  $100^\circ\text{C}$  having been ball milled for 1 h ( $Q_{\text{TR}} = 72.8 \text{ kJ/g}$ )

### 3.4. Isothermal dehydrogenation behavior of ball-milled samples

Figure 17a-c shows dehydrogenation curves at four temperatures for samples ball milled with the injection quantities of milling energy input  $Q_{\text{TR}} = 36.4$ ,  $72.8$  and  $364 \text{ kJ/g}$ , corresponding to the milling duration of 0.5, 1 and 5 h.

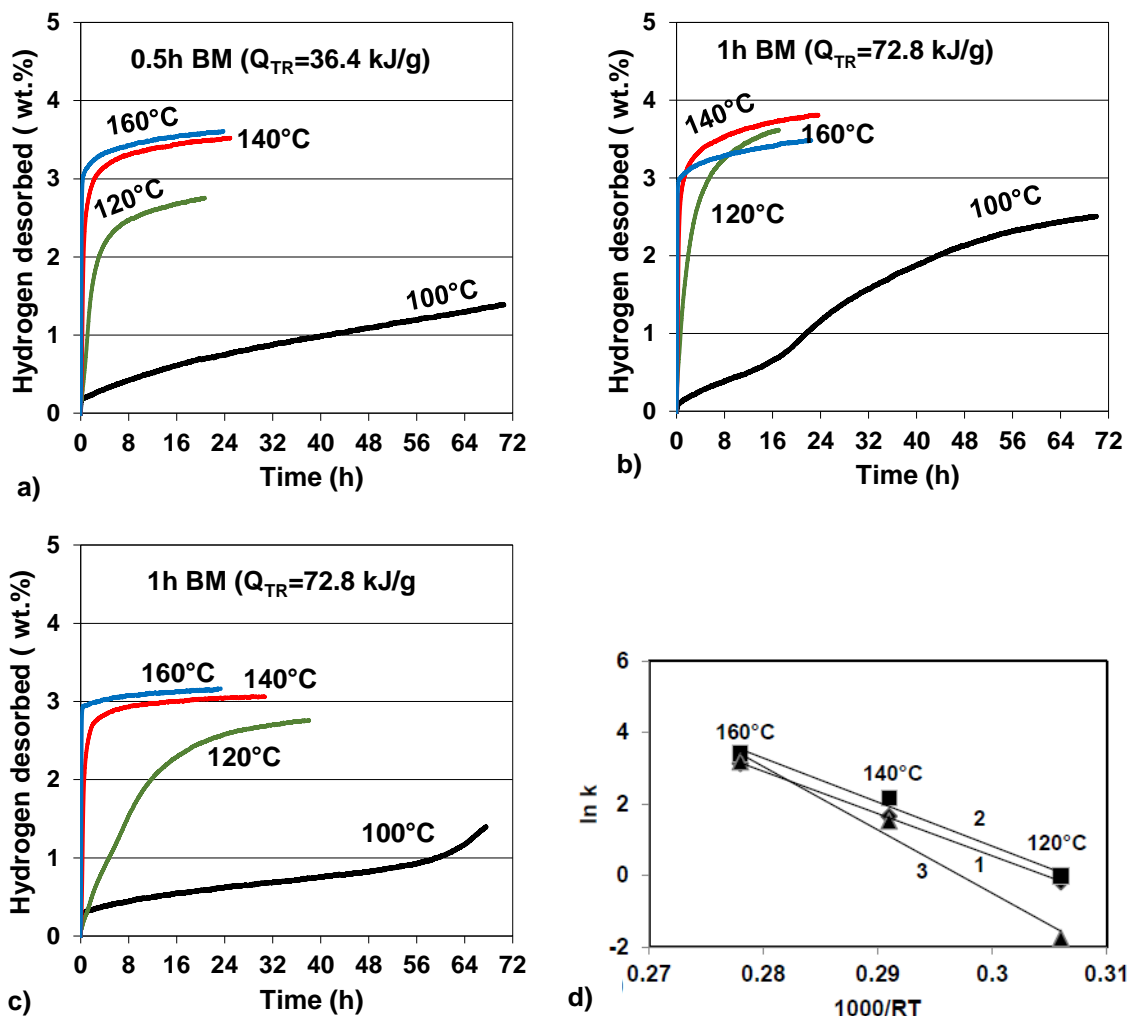


Figure 17: Desorption curves for the  $(2\text{NaBH}_4+\text{MnCl}_2)$  samples milled with increasing milling energy input  $Q_{\text{TR}}$  for (a) 0.5 h;  $Q_{\text{TR}}=36.4$  kJ/g, (b) 1 h;  $Q_{\text{TR}}=72.8$  kJ/g, and (c) 5 h;  $Q_{\text{TR}}=364$  kJ/g. (d) The Arrhenius plots of rate constant  $k$  with temperature for estimation of the apparent activation energy of hydrogen desorption: 1 - 0.5 h BM ( $Q_{\text{TR}}=36.4$  kJ/g):  $y = -118.21x + 36.016$ ,  $R^2=0.9995$ , 2 - 1 h BM ( $Q_{\text{TR}}=72.8$  kJ/g):  $y = -123.09x + 37.754$ ;  $R^2=0.9867$  and 3 - 5 h BM ( $Q_{\text{TR}}=364$  kJ/g):  $y = -177.07x + 52.628$ ;  $R^2=0.9784$ .

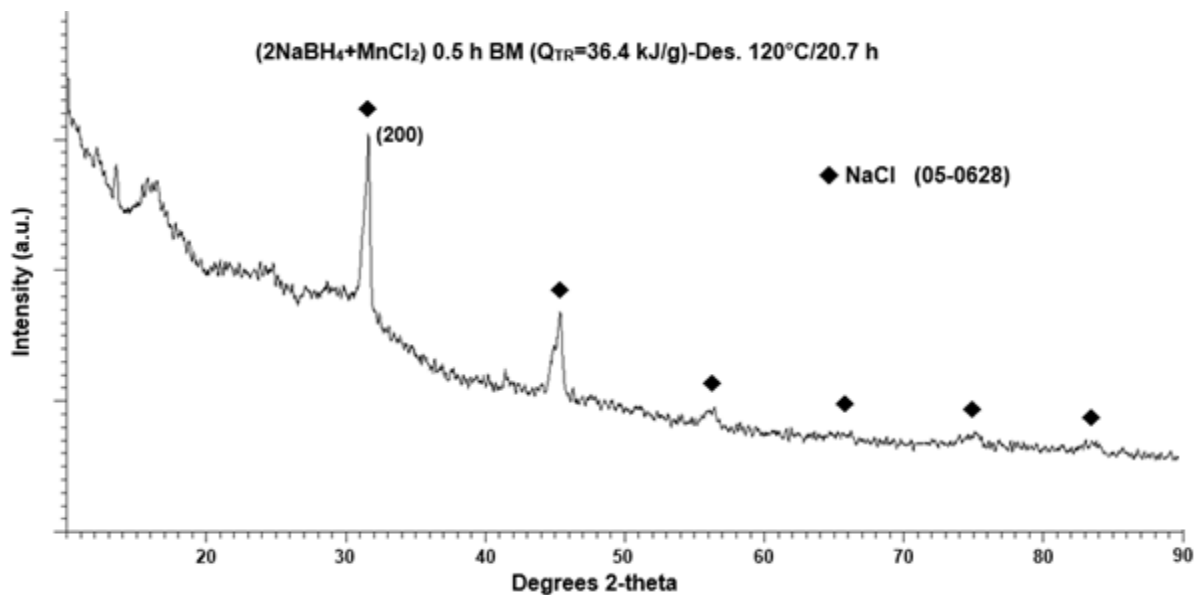
The dehydrogenation process is very characteristic being extremely sluggish at 100°C and then becoming much more rapid when temperature increases by only 20°C, from 100 to 120°C, for the samples milled for 0.5 and 1 h.

For those two samples, the maximum desorbed capacity does not exceed 4 wt. %  $\text{H}_2$  which is very close to the theoretical  $\text{H}_2$  capacity of reaction (3) and strongly supports the notion that

the  $\alpha$ -Mn(BH<sub>4</sub>)<sub>2</sub> hydride was, indeed, synthesized by MCAS. Ball milling with a much larger quantity of injected milling energy input  $Q_{TR}=364$  kJ/g (5 h) makes the rate of dehydrogenation worse as can be seen in *Figure 17c*. Still, the dehydrogenation kinetics at 100°C are very slow but even at a higher temperature range 120-160°C the kinetics is much worse than that in *Figure 17a-b*. *Figure 17d* shows the Arrhenius plots for estimating the apparent activation energies using data for 120, 140 and 160°C. The data for 100°C was not used due to very sluggish dehydrogenation kinetics. Lines 1 and 2 represent samples ball milled for 0.5 h and 1 h for which the estimated activation energies with the experimental error bar equal to  $118.21 \pm 13.55$  and  $123.09 \pm 2.94$  kJ/mol, respectively. Within the experimental error the estimated values are very similar although a larger experimental error bar for the sample milled for 0.5 h implies some inhomogeneity of the ball milled microstructure. In contrast, the apparent activation energy for the sample milled for 5 h is much higher being equal to  $177.07 \pm 20.99$  kJ/mol. The latter value is in an excellent agreement with the sluggish dehydrogenation kinetics observed in *Figure 17c*.

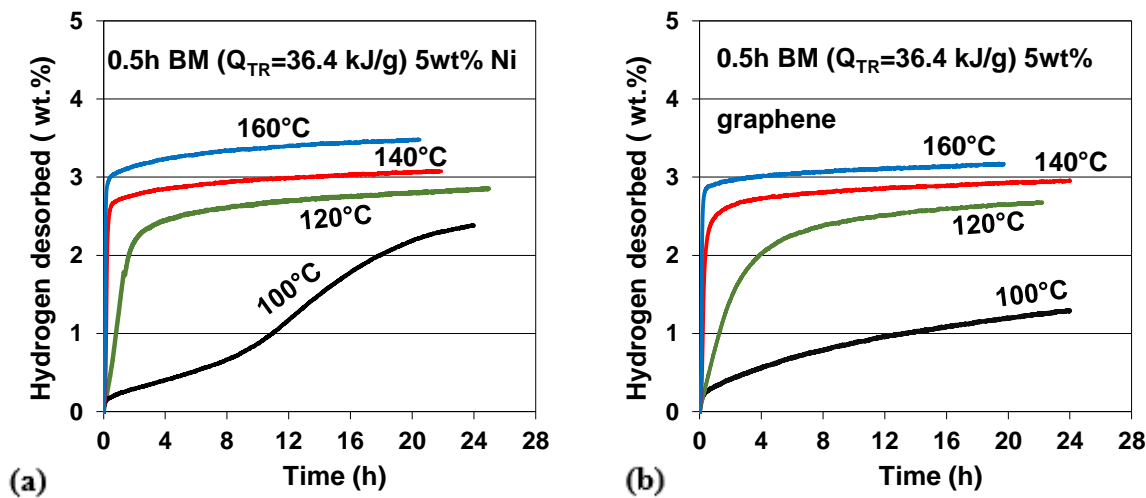
There is a strong correlation between the microstructure observed in *Figure 6* for the sample ball milled for 5 h and its high activation energy for dehydrogenation accompanied by a large experimental error bar. As mentioned earlier, the highly agglomerated granules of individual powder particles which seem to be converted into thin “slabs” of heavily compacted powder are clearly seen. Apparently, this type of microstructure morphology is not conducive for good dehydrogenation kinetics. The overall dehydrogenation kinetics are quite similar for the samples milled for 0.5 and 1 h both of which show a fast initial dehydrogenation rate and the apparent activation energies much lower than that for the 5 h milled sample. *Figure 18* shows the XRD pattern for the 0.5 h ball milled sample after dehydrogenation at 120°C for 20.7 h.

Only the NaCl-type salt diffraction peaks are clearly observed. The XRD pattern is not much changed after dehydrogenation from the ball milled pattern in *Figure 7*.



*Figure 18: XRD pattern of the 0.5 h ball milled sample after isothermal dehydrogenation at 120°C for 20.7 h.*

### 3.5. Isothermal dehydrogenation behavior of ball-milled samples with catalytic additives



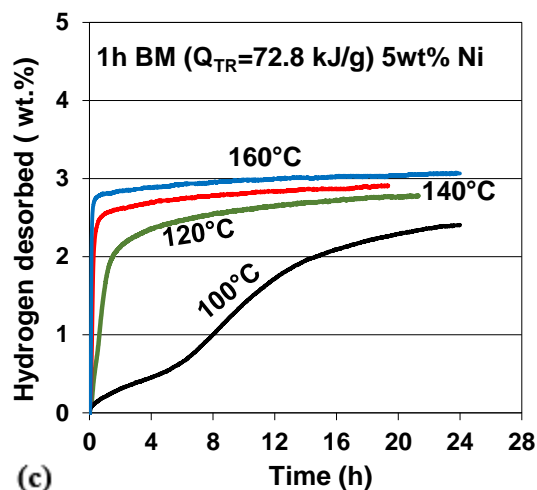


Figure 19: Desorption curves for the  $(2\text{NaBH}_4+\text{MnCl}_2)$  samples milled with additives (a) Ni for 0.5 h;  $Q_{\text{TR}}=36.4$  kJ/g, (b) graphene for 0.5 h;  $Q_{\text{TR}}=36.4$  kJ/g, and (c) Ni for 1 h;  $Q_{\text{TR}}=72.8$  kJ/g.

Ball milling for 5 h ( $Q_{\text{TR}}=364$  kJ/g) was discontinued owing to inferior hydrogen generation performance as compared to milling for 0.5 h ( $Q_{\text{TR}}=36.4$  kJ/g) and 1 h ( $Q_{\text{TR}}=72.8$  kJ/g). Therefore, when additives were used for ball milling, milling times of 0.5 h ( $Q_{\text{TR}}=36.4$  kJ/g) and 1 h (72.8 kJ/g) were used.

Figure 19a-c shows dehydrogenation curves at four temperatures for samples ball milled with additives graphene and ultrafine filamentary nickel for milling energy input  $Q_{\text{TR}}=36.4$  and 72.8 kJ/g, corresponding to the milling duration of 0.5 h and 1 h respectively. A milling time of 1 h was not used for graphene as ultrafine filamentary nickel was selected for further study due to its superior desorption kinetics.

The dehydrogenation process in all three cases is significantly faster compared to Figure 17a-c, although it is still quite sluggish at 100°C. However, performance for the samples milled both for 0.5 and 1 h is two to four times more rapid at 120-160°C compared to Figure 17.

This fact is also evidenced in the reduced apparent activation energy for the powders milled with both additives. The Arrhenius plots in *Figure 20* were used for calculating this. As before, the data for 100°C was not used because of the sluggish kinetics and also to maintain consistency in the comparison of data in *Figure 17* and *Figure 19*.

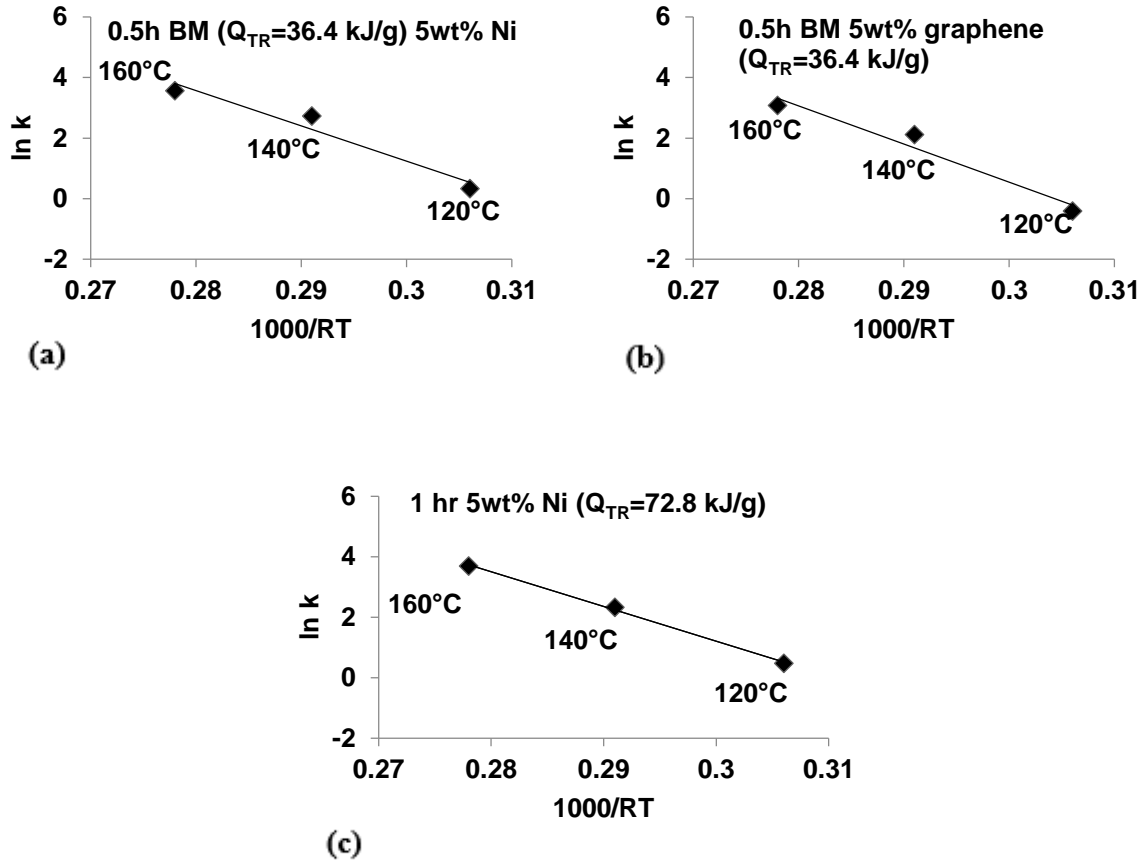


*Figure 20: The Arrhenius plots of rate constant  $k$  with temperature for estimation of the apparent activation energy of hydrogen desorption (a) 0.5 h BM 5 wt. % Ni ( $Q_{TR}=36.4$  kJ/g):  $y= -116.68 + 36.24x$ ,  $R^2=0.948$ , (b) 0.5 h BM 5 wt. % graphene ( $Q_{TR}=36.4$  kJ/g):  $y=-125.93 + 38.323x$ ;  $R^2=0.99553$  and (c) 1 h BM 5 wt. % Ni ( $Q_{TR}=72.8$  kJ/g ):  $y= -115.19 + 35.759x$ ;  $R^2=0.9977$ .*

The estimated activation energies for 0.5 h BM with 5 wt. % Ni, 0.5 h BM with 5 wt. % graphene and 1 h BM with 5 wt. % Ni, with the experimental error bar, were equal to  $116.68 \pm 15.1$ ,  $125.93 \pm 13.44$  and  $115.19 \pm 11.31$  kJ/mol, respectively. These results show that the

degree of inhomogeneity for the three samples was fairly large, but very similar. The values compare well with the dehydrogenation kinetics observed in *Figure 19a-c*.

### 3.6. Isothermal dehydrogenation of ball-milled samples doped with LiNH<sub>2</sub>

*Figure 21* shows dehydrogenation curves at four temperatures for samples ball milled with 5 wt. % LiNH<sub>2</sub> for milling energy input  $Q_{TR}=36.4$  kJ/g, corresponding to the milling duration of 0.5 h.

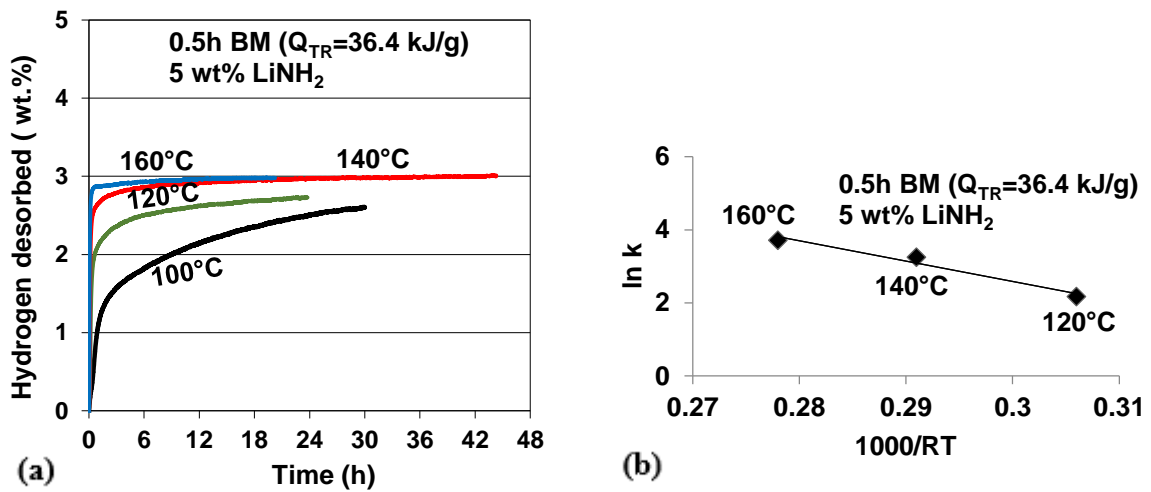


*Figure 21: (a) Desorption curves for the (2NaBH<sub>4</sub>+MnCl<sub>2</sub>)+5 wt. % LiNH<sub>2</sub> samples milled for 0.5 h ( $Q_{TR}=36.4$  kJ/g);; (b) the Arrhenius plots of rate constant  $k$  with temperature for estimation of the apparent activation energy of hydrogen desorption for 0.5 h BM, 5 wt. % LiNH<sub>2</sub> ( $Q_{TR}=36.4$  kJ/g):  $y = -55.61 \pm 19.269$ ,  $R^2=0.967$*

The estimated activation energy for 0.5 h BM with 5 wt. % LiNH<sub>2</sub> was equal to  $55.61 \pm 4.97$  kJ/mol.

From the figure, it can be observed that doping with LiNH<sub>2</sub> improves desorption performance significantly, and to a greater degree than catalytic additives graphene and Ni. Most significantly, there is a marked increase in desorption kinetics at 100°C. However, the quantity of H<sub>2</sub> desorbed is suppressed to a level below than that desorbed by the powders with the catalytic additives.

This is supported by *Figure 21(b)*, used to calculate the apparent activation energy, which was found to be lowered by more than 50% in comparison to the next lowest observed value, which was with Ni.

### ***3.7. Thermal (thermodynamic) behaviour of ball milled samples in DSC/TGA and gas mass spectrometry (MS)***

*Figure 22a-b* shows the results of gas mass spectrometry (MS) for a powder sample (A), ball milled for 0.5 h with a low input of milling energy. It is clearly seen that together with a principal H<sub>2</sub> gas desorption peak (black curve), which starts desorbing at ~75°C and reaches a peak maximum at ~150°C, there appears a much smaller peak of diborane B<sub>2</sub>H<sub>6</sub> (blue curve) that commences at ~135°C and terminates at ~175°C with a peak maximum ~160°C. Therefore, the threshold temperature for the end of B<sub>2</sub>H<sub>6</sub> release is assumed to be 200°C for further analysis. The ratio of the peak intensity of H<sub>2</sub> to diborane (B<sub>2</sub>H<sub>6</sub>) up to 200°C is H<sub>2</sub>/B<sub>2</sub>H<sub>6</sub>=948 in *Figure 22a*. A smaller H<sub>2</sub> peak is also observed around 450°C in *Figure 22a* which, most likely, is related to the decomposition of retained NaBH<sub>4</sub> in the ball milled microstructure.

*Figure 22b* shows thermogravimetric (TGA) and differential scanning calorimetry (DSC) results for the first sample (A) extracted from the 0.5 h milled powder. A rapid TG mass loss (black curve) occurs within a narrow temperature range and equals to 5.06 wt. % up to 200°C. Beyond 200°C there is still a very slow TG mass loss, most likely, related to a gradual decomposition of retained NaBH<sub>4</sub> but not to the release of B<sub>2</sub>H<sub>6</sub> which was terminated at 200°C as mentioned above. An endothermic peak on a DSC curve (blue) centered at ~160°C, is observed. Another very broad endothermic peak is observed at 450-475°C which corresponds to the MS peak at the same temperature range (*Figure 22a*) and is due to the decomposition of

retained  $\text{NaBH}_4$  being in agreement with TGA. The broken red line in *Figure 22b* shows a first derivative of the TG line ( $d\text{TG}/dT$  where T - temperature). It very precisely indicates the range of temperatures within which the mass loss occurs and clearly confirms that the TG mass loss in *Figure 22b* is related to the occurrence of the endo peak at  $\sim 160^\circ\text{C}$ . Therefore, the release of  $\text{H}_2$  gas containing a small amount of  $\text{B}_2\text{H}_6$  is an endothermic event resulting in a mass loss of 5.06 wt. % up to  $200^\circ\text{C}$  in *Figure 22b*.

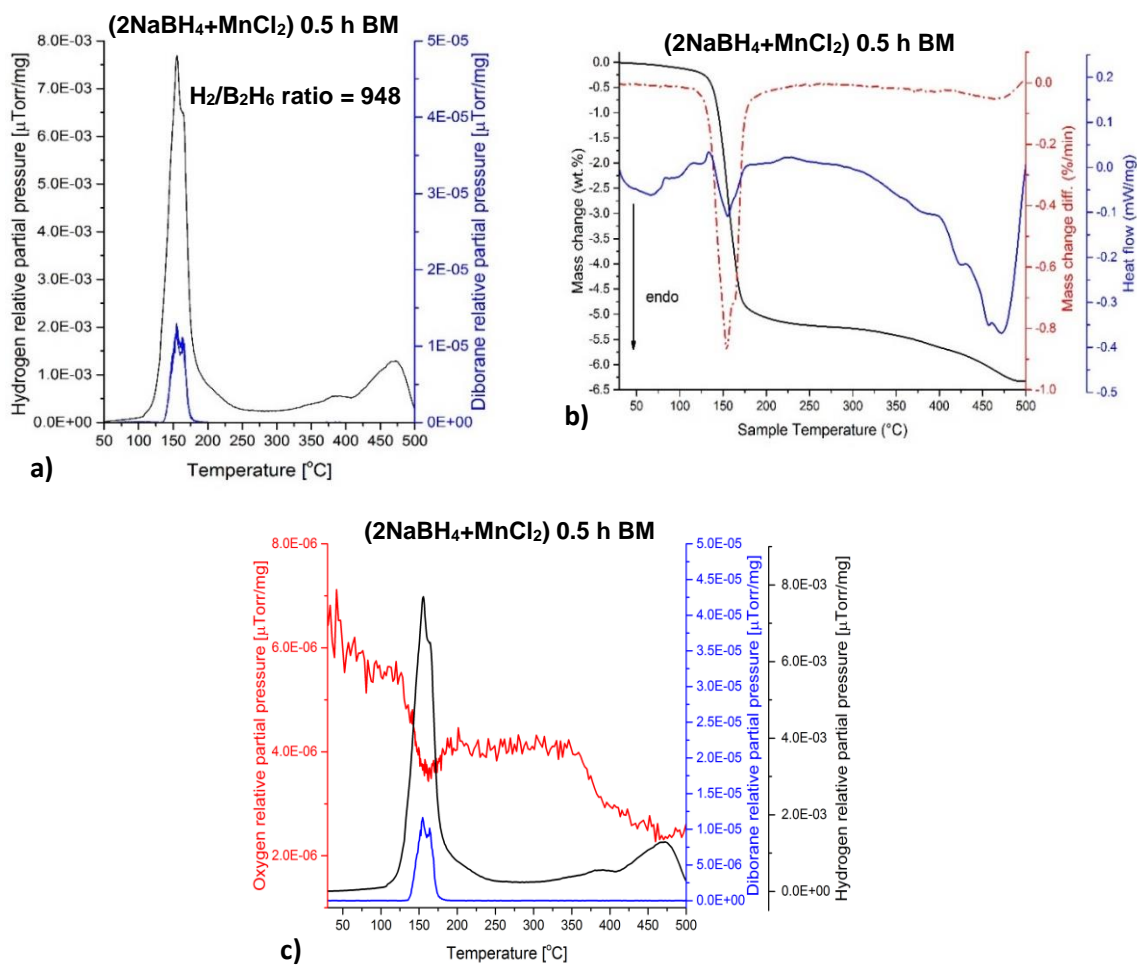
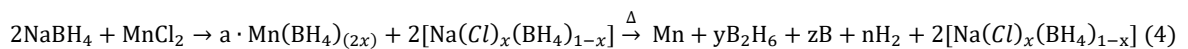


*Figure 22: (a) Mass spectrometry (MS) gas desorption spectra for a  $(2\text{NaBH}_4+\text{MnCl}_2)$  sample ball milled for 0.5 h ( $Q_{TR}=36.4$  kJ/g). (b) TG and DSC curves and (c) the change in the partial pressure of oxygen during desorption of a  $(\text{H}_2+\text{B}_2\text{H}_6)$  gas mixture. Heating rate  $5^\circ\text{C}/\text{min}$ .*

As mentioned above, in order to confirm the correctness of the TGA/DSC results in *Figure 22b*, a second sample (B) extracted from the same 0.5 h milled powder was also investigated. The TGA/DSC were nearly identical exhibiting a mass loss of 4.31 wt. % up to 200°C as in *Figure 22b* in an endothermic event. Also investigated was a gas release from this sample (see *Appendix E*) which showed a very similar pattern to that in *Figure 22a* with the peak intensity ratio  $H_2/B_2H_6 = 735$ . An important finding is that in the endothermic gas release event in *Figure 22a-b*, there is also a small amount of  $B_2H_6$  recorded by the MS apparatus in a mixture with a principal  $H_2$  gas. Interestingly, the peak intensity ratio  $H_2/B_2H_6$  for sample (A) and (B) of the same 0.5 h milled powder is 948 with 5.06 wt. % TG loss and 735 with 4.31 wt. % TG loss, respectively. It is to be pointed out that one cannot make any direct correlation between the  $H_2/B_2H_6$  ratios and the quantity of  $B_2H_6$  released since the ratios are only calculated from the mass normalized MS peak areas and do not take into account the molecular masses of released species. However, the ratio difference between both samples is a good indicator that the quantity of released  $B_2H_6$  is relatively small.

By analogy to the ball milled ( $2LiBH_4 + MnCl_2$ ) system, it is suggested that the dehydrogenation/decomposition reaction for the ball milled ( $2NaBH_4 + MnCl_2$ ) mixture can be presented in the following general form:



Unfortunately, the estimate of the exact values of x, y, z and n is not possible. The suggested general dehydrogenation reaction (4) requires the formation of the elemental Mn metal. The Mn diffraction peaks are not observed in *Figure 18* in the XRD pattern for the 0.5 h ball milled sample after dehydrogenation at 120°C for 20.7 h which suggests that Mn could be amorphous. In contrast to reaction described by equation (4), Guda et al. [24] suggested that the thermolysis

of  $\text{Mn}(\text{BH}_4)_2$  occurs through the formation manganese borides  $\text{Mn}_2\text{B}$ ,  $\text{MnB}$ , or  $\text{MnB}_4$ . They based their conclusion on the theoretical calculations of the Mn K-edge XANES spectra of different manganese borides. However, from the metallurgical viewpoint, the formation of manganese borides at low temperatures ( $\sim 100^\circ\text{C}$ ), at which the decomposition of  $\text{Mn}(\text{BH}_4)_2$  occurs, is highly unlikely because manganese borides require very high temperatures ( $>900^\circ\text{C}$ ) and high pressures for their formation [32, 33].

Finally, it must be pointed out that the observations presented here clearly indicate the release of diborane gas from  $\alpha\text{-Mn}(\text{BH}_4)_2$  similar to its crystalline counterpart.

### 3.8. Thermal (thermodynamic) behaviour of ball milled samples with graphene additive in DSC/TGA and gas mass spectrometry (MS)

To study the nature and quantity of the gas species released during the desorption of the 0.5 h ball milled powder with 5 wt. % graphene, a randomly chosen sample was analyzed by mass spectrometry (MS) and DSC/TGA. Figure 23a-b shows the results.

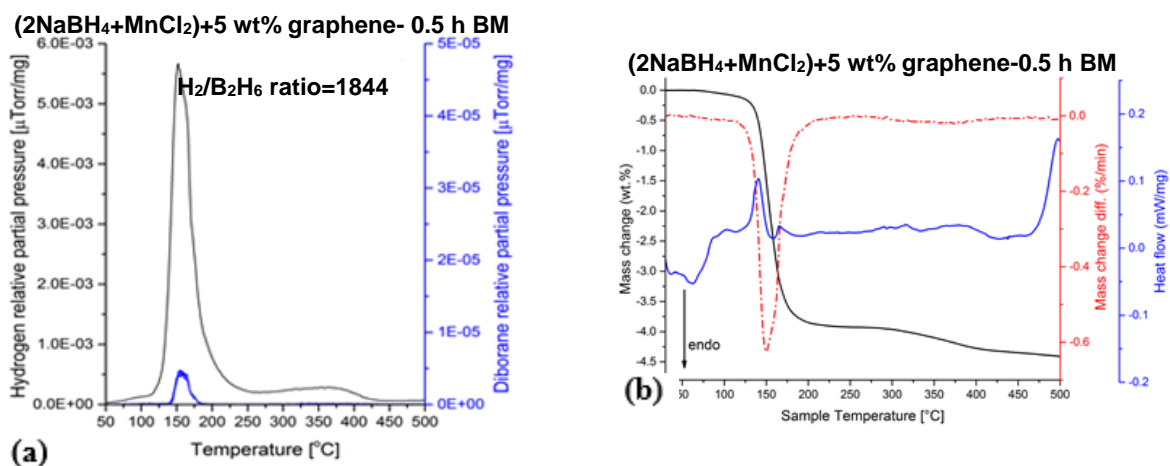


Figure 23: (a) Mass spectrometry (MS) gas desorption spectra for a  $(2\text{NaBH}_4+\text{MnCl}_2)+5$  wt. % graphene sample ball milled for 0.5 h ( $Q_{\text{TR}}=36.4$  kJ/g). (b) TG and DSC curves during desorption of a  $(\text{H}_2+\text{B}_2\text{H}_6)$  gas mixture. Heating rate  $5^\circ\text{C}/\text{min}$ .

In *Figure 23a*, the black curve with a principal H<sub>2</sub> gas desorption peak starts desorbing at ~50°C and reaches a peak maximum at ~150°C. Simultaneously, a small peak of diborane, B<sub>2</sub>H<sub>6</sub>, (blue curve) commences at ~135°C and terminates at ~175°C with a peak maximum ~160°C, which is very similar to the nature of the curve observed in *Figure 22a*. However, the ratio of the peak intensity of H<sub>2</sub> to diborane (B<sub>2</sub>H<sub>6</sub>) up to 200°C, H<sub>2</sub>/B<sub>2</sub>H<sub>6</sub> = 1844 in *Figure 23a* compared to 948 in *Figure 22a*. It is also observed that the smaller H<sub>2</sub> peak is observed around 450°C in *Figure 22a* is absent in *Figure 23a*, which indicates that ball milling the powder mixture with 5 wt. % graphene leads to a complete reaction of NaBH<sub>4</sub> with MnCl<sub>2</sub>.

*Figure 23b* shows thermogravimetric (TGA) and differential scanning calorimetry (DSC). A very rapid TG mass loss (black curve) occurs within a narrow temperature range and equals to 3.8 wt. % up to 200°C. An exothermic peak is observed on the DSC curve (blue) centered at ~135°C, which corresponds very well to the start of the release of diborane. An endothermic event follows immediately afterwards, suggesting the release of H<sub>2</sub> gas and a very small amount of B<sub>2</sub>H<sub>6</sub>. Research in our lab, which is yet to be published, has shown that graphene when ball milled decomposes into a highly dispersed amorphous carbon [34]. It is hypothesized that the exothermic event is due to the reaction of this amorphous carbon with B<sub>2</sub>H<sub>6</sub> released from the mixture during heating. This is evidenced in the reduction of the B<sub>2</sub>H<sub>6</sub> peak in *Figure 23a*, which increased H<sub>2</sub>/B<sub>2</sub>H<sub>6</sub> ratios two-fold from 948 in *Figure 22a* to 1844 in *Figure 23a*. This is consistent with the first derivative of the TG line (broken red line) in *Figure 23b* which indicates the range of temperatures within which the mass loss occurs. It begins and ends with the endothermic event. A follow-up experiment was also conducted in which the H<sub>2</sub>/B<sub>2</sub>H<sub>6</sub> ratio was 1256. *Appendix E* shows the results of the follow-up experiments conducted in which the H<sub>2</sub>/B<sub>2</sub>H<sub>6</sub> ratio of 1256.

### 3.9. Thermal (thermodynamic) behaviour of ball milled samples with LiNH<sub>2</sub> additive in DSC/TGA and gas mass spectrometry (MS)

As shown in *Figure 24a* below, ball milling with lithium amide, LiNH<sub>2</sub>, almost completely eliminates the release of diborane, B<sub>2</sub>H<sub>6</sub>. The H<sub>2</sub>/B<sub>2</sub>H<sub>6</sub> peak ratio in *Figure 24a* up to 200°C is 5001.

*Figure 24b* shows that desorption of H<sub>2</sub> and the suppression of the release of B<sub>2</sub>H<sub>6</sub> is collectively an exothermic event. The exothermic peak begins at ~110°C and ends at ~150°C. As in the above subsection, it is thought that this can be attributed to LiNH<sub>2</sub> reacting with B<sub>2</sub>H<sub>6</sub>.

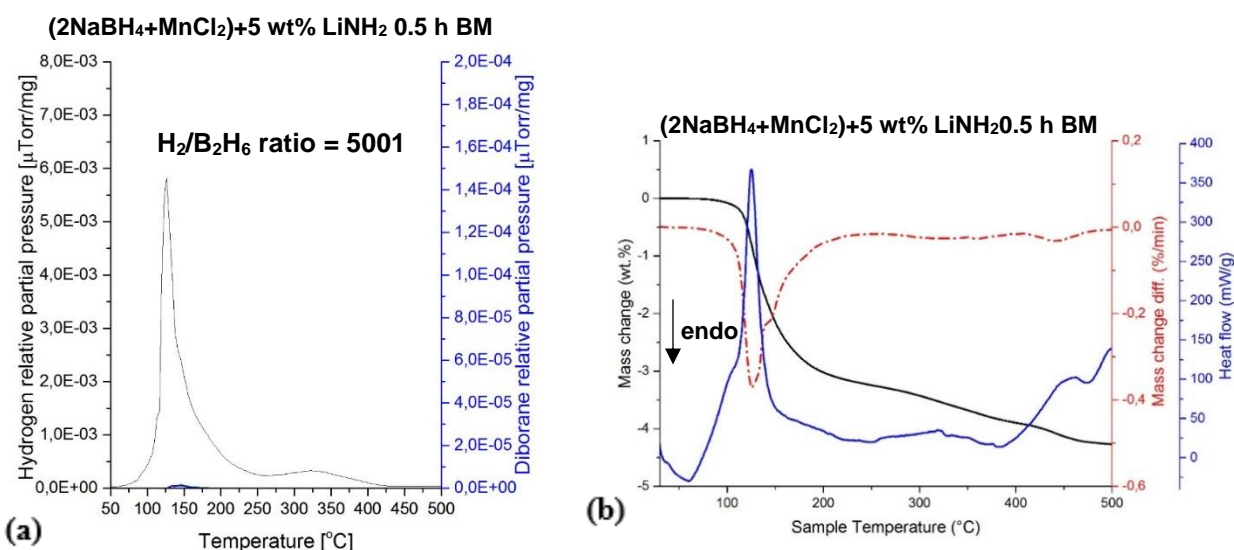


*Figure 24: (a) Mass spectrometry (MS) gas desorption spectra for a (2NaBH<sub>4</sub>+MnCl<sub>2</sub>) + 5 wt. % LiNH<sub>2</sub> sample ball milled for 0.5 h ( $Q_{TR}$ =36.4 kJ/g). (b) TG and DSC curves during desorption of a (H<sub>2</sub>+B<sub>2</sub>H<sub>6</sub>) gas mixture. Heating rate 5°C/min.*

It is postulated that one of the two following reactions may be occurring leading to the exothermic event in *Figure 24b* since both have a net negative enthalpy of reaction (see *Appendix D*) assuming that 1 mol of B<sub>2</sub>H<sub>6</sub> reacts:





Equation (6) appears more likely because it appears from *Figure 24b* that the sample desorbs in two stages: ~ 3 wt. % H<sub>2</sub> rapidly from ~100°C to ~200°C and ~1 wt. % H<sub>2</sub> from ~200°C until the end of the test. It is likely that the second stage is due to the decomposition of LiBH<sub>4</sub> produced as a result of reaction (6). *Appendix C* shows the results of two follow-up experiments conducted in which the H<sub>2</sub>/B<sub>2</sub>H<sub>6</sub> ratios were 5198 and 4456.

### **3.10.      *Microstructure of crystalline Mn(BH<sub>4</sub>)<sub>2</sub> produced by solvent extraction/filtration***

As mentioned earlier, the NaCl-type salt which is formed as a by-product of the general, solid state “metathesis” reaction (3), is completely useless being a “dead-weight” which adds up to the total molecular weight of the synthesized (a-Mn(BH<sub>4</sub>)<sub>(2x)</sub>+2Na(Cl)<sub>x</sub>(BH<sub>4</sub>)<sub>(1-x)</sub>) mixture and reduces the gravimetric H<sub>2</sub> desorption capacity and as such, should be eventually removed from the material. We attempted to separate a-Mn(BH<sub>4</sub>)<sub>(2x)</sub> from 2NaCl<sub>x</sub>(BH<sub>4</sub>)<sub>(1-x)</sub> using the solvent extraction/filtration as described in *Chapter 2*.

In contrast to a pale brown color of the ball milled mixture, the dry powder obtained after solvent extraction had light grey colour, which is a completely different colour from the pale yellow color of the Mn(BH<sub>4</sub>)<sub>2</sub>.NaBH<sub>4</sub> mixture obtained in the final drying step of the solvent synthesis route [35].

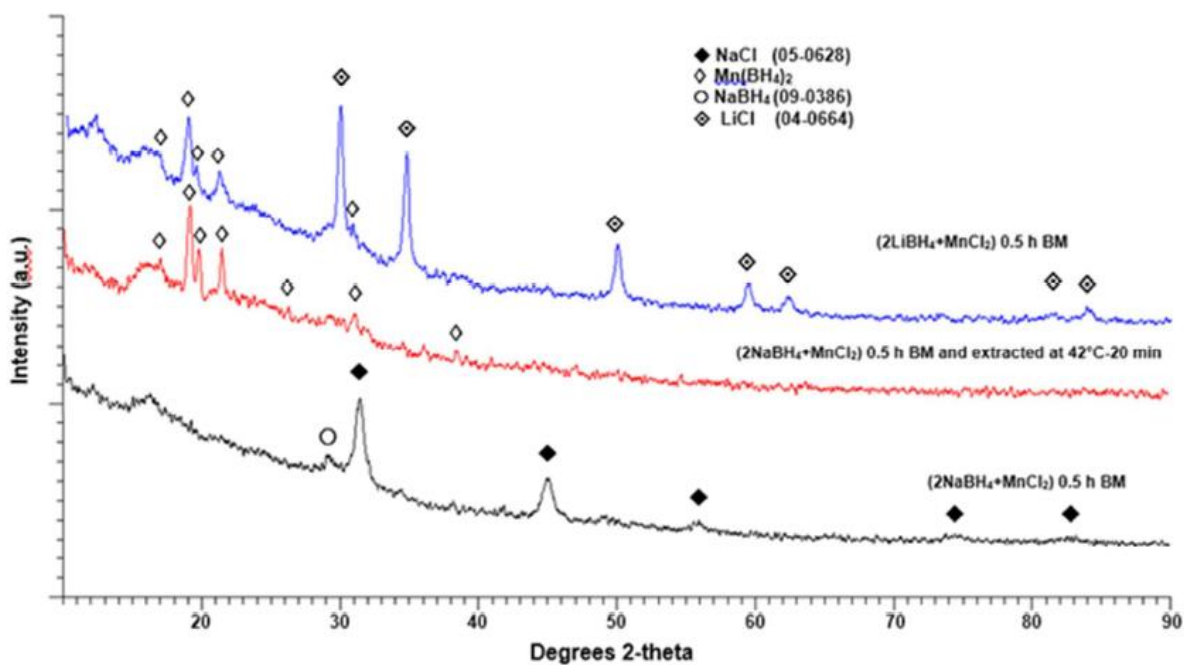


Figure 25: XRD patterns of the 0.5 h BM sample, solvent extracted at 42°C for 20 min (center) in comparison to the XRD patterns of the 0.5 h BM (2NaBH<sub>4</sub>+MnCl<sub>2</sub>) (bottom) and (2LiBH<sub>4</sub>+MnCl<sub>2</sub>) (top) samples.

Figure 25 shows a comparison of the XRD patterns for the (2NaBH<sub>4</sub>+MnCl<sub>2</sub>) mixture after ball milling (bottom), the same mixture after solvent extraction at 42°C as described in the Chapter 2 (center) and the (2LiBH<sub>4</sub>+MnCl<sub>2</sub>) mixture after ball milling (top). It is clearly seen that as discussed earlier, the XRD pattern for the ball milled (2NaBH<sub>4</sub>+MnCl<sub>2</sub>) exhibits only the NaCl-type diffraction peaks and a weak, singular NaBH<sub>4</sub> peak. Surprisingly, the XRD pattern of the same mixture after solvent extraction is nearly identical to the XRD pattern of the ball milled (2LiBH<sub>4</sub>+MnCl<sub>2</sub>) mixture in which the crystalline Mn(BH<sub>4</sub>)<sub>2</sub> hydride co-existing with 2LiCl was formed. There are no NaCl-type diffraction peaks seen on the XRD pattern for the solvent extracted powder because the NaCl-type salt was quite effectively filtered during the extraction procedure as shown in Figure 25. It is quite clear that during solvent extraction, disordered  $\alpha$ -Mn(BH<sub>4</sub>)<sub>2</sub>, which was formed through ball milling, is

transformed into crystalline  $\text{Mn}(\text{BH}_4)_2$ . Identical results were observed when 1 h ball milled  $(2\text{NaBH}_4+\text{MnCl}_2)$  was used.

Figure 26 below shows that similar result was observed when the ball milled  $(2\text{NaBH}_4+\text{MnCl}_2)+5\text{wt. \% Ni}$  was extracted. The same types of peaks associated with crystalline  $\text{Mn}(\text{BH}_4)_2$  in Figure 25 are observed, but their intensities are slightly stronger, making them clearly discernable from the noise. Interestingly, no Ni peaks are observed in the pattern, which strongly suggests that the ultrafine filamentary Ni did not pass through the syringe filter during extraction. Thus, the catalytic effect of Ni was not observed in the hydrogen desorption characteristics of this powder, and the results were archived.

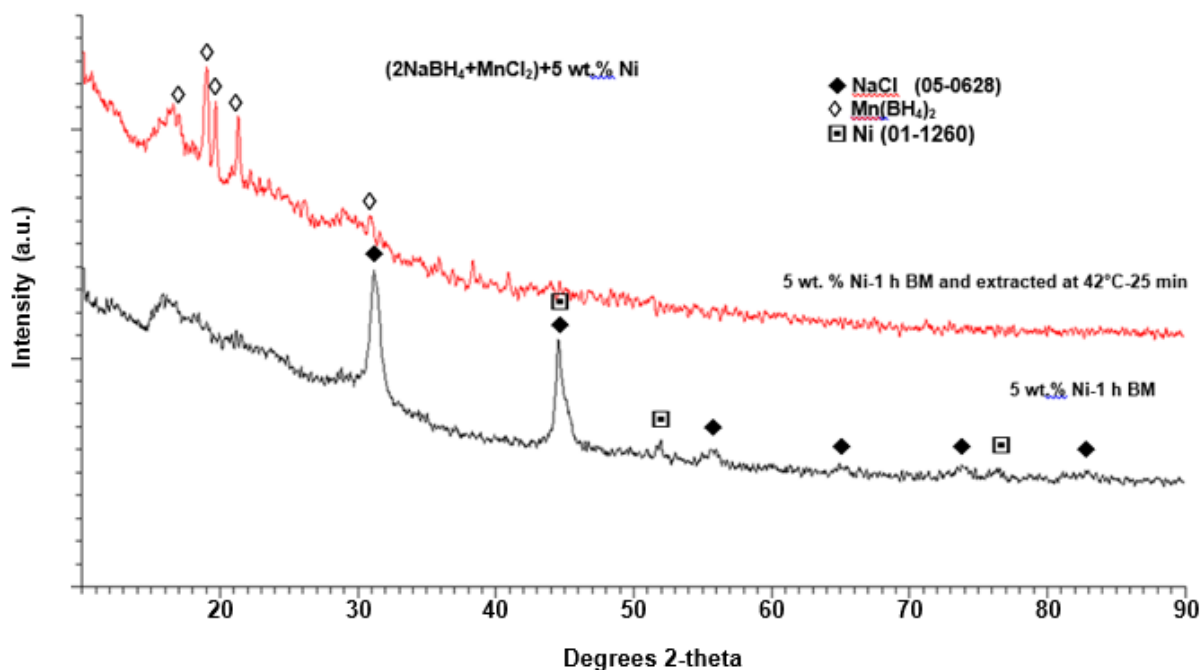


Figure 26: XRD patterns of the 1 h BM ball milled  $(2\text{NaBH}_4+\text{MnCl}_2)+5\text{wt. \% Ni}$  sample, solvent extracted at  $42^\circ\text{C}$  for 25 min (top) in comparison to the XRD patterns of the same ball milled powder before extraction (bottom).

<b>Calculated <math>d_{(hkl)}</math> (Å) for crystalline <math>Mn(BH_4)_2</math> in <math>(2LiBH_4+MnCl_2)</math> from the Bragg's law using data and <math>\lambda=0.73065</math> Å from [16] for synchrotron radiation</b>	<b>Experimental <math>d_{(hkl)}</math> (Å) for crystalline <math>Mn(BH_4)_2</math> from SAEDP [36] in <math>(2LiBH_4+MnCl_2)</math></b>	<b>Experimental <math>d_{(hkl)}</math> (Å) for extracted crystalline <math>Mn(BH_4)_2</math> in <math>(2NaBH_4+MnCl_2)</math> 0.5 h BM; EXT 42°C-20 min [this work]</b>	<b>Experimental <math>d_{(hkl)}</math> (Å) for extracted crystalline <math>Mn(BH_4)_2</math> in <math>(2NaBH_4+MnCl_2)</math> 1 h BM; EXT 42°C-25 min (this work)</b>
<b><math>d_{(hkl)}</math> (Å)</b>	<b><math>d_{(hkl)}</math> (Å)</b>	<b><math>d_{(hkl)}</math> (Å)</b>	<b><math>d_{(hkl)}</math> (Å)</b>
8.883	---	-	-
-	-	-	5.310
5.242	---	5.207	5.184
-	-	-	4.887
4.689	---	4.623	4.635
4.552	---	4.476	4.487
4.185	---	4.134	4.148
3.961	---	-	3.984
-	-	-	3.888
3.461	3.46	-	-
3.438	3.43	3.389	-
2.923	2.89	2.872	2.881

*Table 5: Experimental lattice spacings,  $d_{(hkl)}$ , for crystalline, extracted  $Mn(BH_4)_2$  obtained in this work from the 0.5 h and 1 h ball milled  $(2NaBH_4+MnCl_2)$  mixtures, compared to  $d_{(hkl)}$  values calculated from synchrotron radiation [16] and to the experimental ones obtained from SAEDP (selected area electron diffraction pattern) in [36].*

Table 5 shows the XRD derived experimental lattice spacings,  $d_{(hkl)}$ , for crystalline, solvent extracted  $Mn(BH_4)_2$  obtained in this work from the 0.5 h ball milled  $(2NaBH_4+MnCl_2)$  mixture, as compared to the  $d_{(hkl)}$  values calculated from synchrotron radiation and to the experimental  $d_{(hkl)}$  values obtained from SAEDP (selected area electron diffraction pattern) in [36]. The experimental  $d_{(hkl)}$  spacings are in a very good agreement with those reported in [16, 36]. A small difference in the spacing values may arise from different precursors used for the  $Mn(BH_4)_2$  synthesis and slightly different conditions for the synthesis used in this work and [16, 36].

The mechanism of transformation from an amorphous to crystalline  $\text{Mn}(\text{BH}_4)_2$  hydride after ball milling and subsequent solvent extraction is not well understood. So far, it has never been reported in literature.

### 3.11. Isothermal desorption behavior of the extracted sample

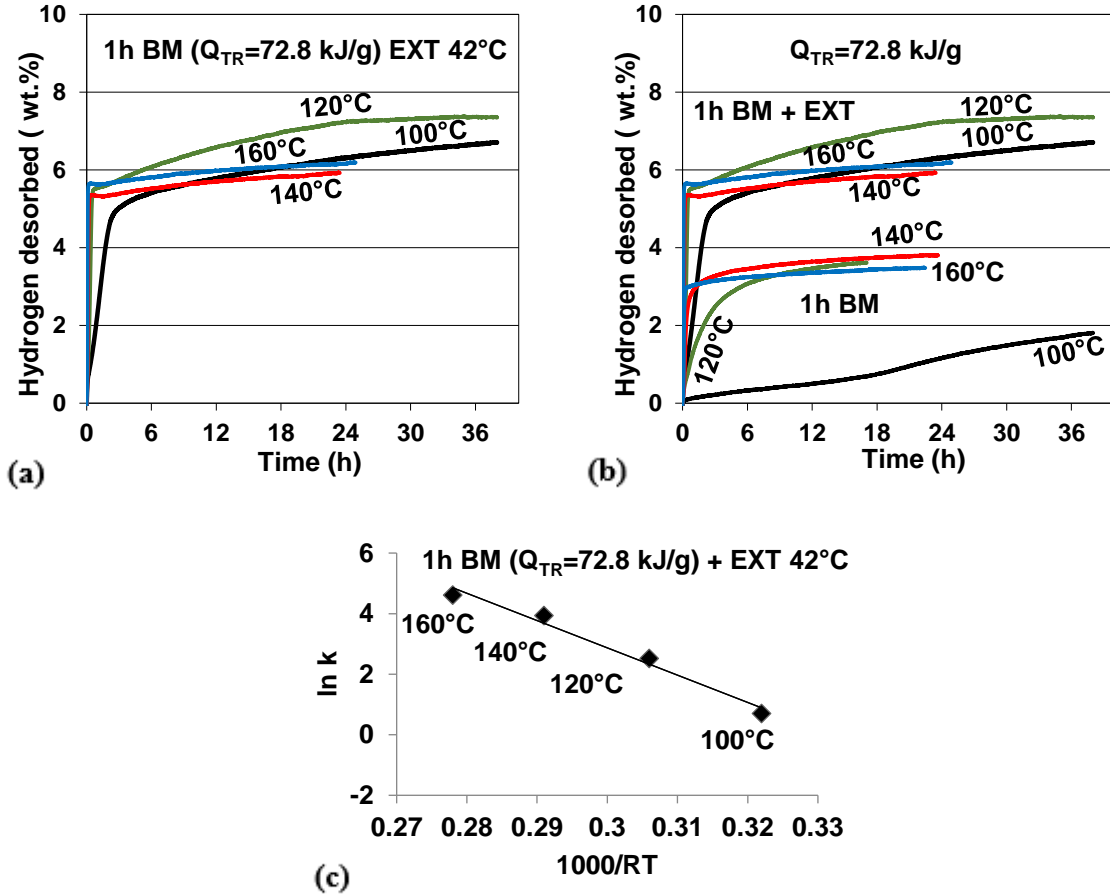


Figure 27: Desorption curves for the  $(2\text{NaBH}_4+\text{MnCl}_2)$  samples milled with a milling energy input  $Q_{TR}=72.8$  kJ/g for 1 h (a) after extraction, and (b) showing the effect of the extraction procedure, while (c) shows the Arrhenius plot of rate constant  $k$  with temperature for estimation of the apparent activation energy of hydrogen desorption: 1 h BM and extracted ( $Q_{TR}=72.8$  kJ/g):  $y = -90.15x + 29.914$ ;  $R^2 = 0.9784$ .

Figure 27a-c shows that the removal of NaCl during the solvent extraction process has drastically improved the hydrogen desorption performance of the sample.

The gravimetric capacity of the powder increased from ~3.7 wt. % (1 h BM, 120°C) to ~7.3 wt. % (1 h BM extracted, 120°C). This is still significantly below the theoretical ~9.5 wt. % gravimetric capacity of pure Mn(BH<sub>4</sub>)<sub>2</sub>. This anomaly could be explained by the fact that the microstructure of the extracted powder (Figure 20) resembles the thin “slabs” of highly compacted powder (Figure 6a-b) that exhibited poor desorption characteristics for the high energy ball milled sample in Figure 17c (5 h, Q<sub>TR</sub>=364 kJ/g). The exact effect of this apparent agglomeration is not completely understood, apart from the fact that it is detrimental to powder desorption kinetics.

However, the desorption process was rapid at 100°C, unlike the sluggishness observed in every sample that was not extracted. Therefore, the Arrhenius plot used the data obtained at this temperature for calculating the apparent activation energy of the sample, as shown in Figure 27c.

The apparent activation energy of the sample with experimental error bar was estimated to be 90.15 ± 14.61 kJ/mol, which, as expected, is lower than all of the ball milled samples with or without the addition of catalysts, and demonstrates a moderate degree of inhomogeneity.

### **3.12. Thermal (thermodynamic) behaviour of (2NaBH<sub>4</sub>+MnCl<sub>2</sub>) sample ball milled for 1 h and extracted at 42°C**

Figure 28a shows that the desorption of the isolated crystalline Mn(BH<sub>4</sub>)<sub>2</sub> results in drastically reduced release of B<sub>2</sub>H<sub>6</sub> compared to that observed for a-Mn(BH<sub>4</sub>)<sub>2</sub> in Figure 22a. The H<sub>2</sub>/B<sub>2</sub>H<sub>6</sub> ratio for this sample is in the range of 1500-1600 versus 700-900 for a-Mn(BH<sub>4</sub>)<sub>2</sub>. The MS/TGA curves in Figure 28b are difficult to interpret as they show the occurrence of a combination of exothermic and endothermic reactions.

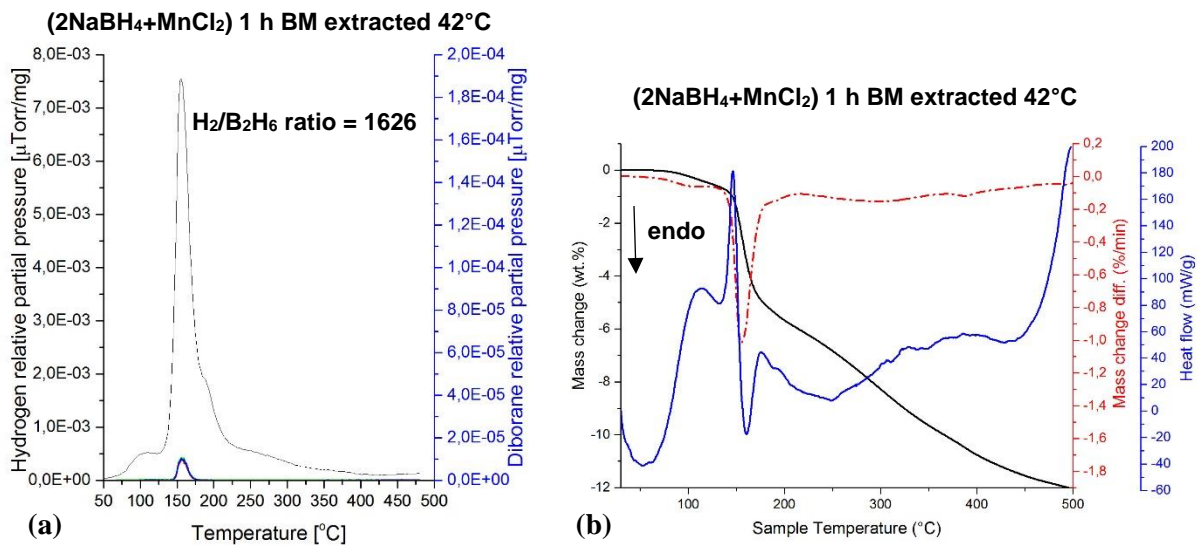


Figure 28: (a) Mass spectrometry (MS) gas desorption spectra for a (2NaBH<sub>4</sub>+MnCl<sub>2</sub>) sample ball milled for 1 h ( $Q_{TR}=72.8$  kJ/g) and then extracted at 42°C using solvent filtration method. (b) TG and DSC curves during desorption of a (H<sub>2</sub>+B<sub>2</sub>H<sub>6</sub>) gas mixture. Heating rate 5°C/min.

#### 4. Conclusions

1. The XRD pattern of the ball milled ( $2\text{NaBH}_4+\text{MnCl}_2$ ) mixture exhibits only the diffraction peaks of a NaCl type salt in contrast to a similar ball milled ( $\text{Mn}(\text{BH}_4)_2+2\text{LiCl}$ ) mixture, synthesized from the  $\text{LiBH}_4$  precursor, which exhibits the diffraction peaks of crystalline  $\text{Mn}(\text{BH}_4)_2$  and those of a LiCl salt. Apparently, mechano-chemical activation synthesis (MCAS) by ball milling of the ( $2\text{NaBH}_4+\text{MnCl}_2$ ) mixture for 0.5 to 5 h produced most likely an *amorphous* manganese borohydride,  $\text{a-Mn}(\text{BH}_4)_2$  accompanied by a NaCl-type salt by product which on the basis of the X-ray diffraction results, could be a solid solution  $\text{Na}(\text{Cl})_x(\text{BH}_4)_{(1-x)}$ .
2. The FT-IR spectrum of the ( $\text{a-Mn}(\text{BH}_4)_{(2x)}+2\text{Na}(\text{Cl})_x(\text{BH}_4)_{(1-x)}$ ) mixture synthesized by MCAS is similar to its counterpart ball milled ( $\text{Mn}(\text{BH}_4)_2+2\text{LiCl}$ ) mixture using  $\text{LiBH}_4$  as a reactant, containing crystalline manganese borohydride,  $\text{c-Mn}(\text{BH}_4)_2$ .
3. Amorphous borohydride,  $\text{a-Mn}(\text{BH}_4)_{(2x)}$ , in the mixture with  $2\text{Na}(\text{Cl})_x(\text{BH}_4)_{(1-x)}$ , which is a “dead weight” by-product, is capable of desorbing up to 3-4 wt. %  $\text{H}_2$  at the temperature range 120-160°C.
4. Catalytic additives, 5 wt. % graphene and 5 wt. % Ni, reduce the onset of desorption from 120°C to 100°C and speed up the desorption kinetics at these temperatures two to four fold.
5. Mass spectrometry (MS) of gas released in the TGA/DSC experiments from the ( $\text{a-Mn}(\text{BH}_4)_{(2x)}+2\text{Na}(\text{Cl})_x(\text{BH}_4)_{(1-x)}$ ) mixture, synthesized by MCAS, indicates mainly hydrogen with a small content of diborane gas,  $\text{B}_2\text{H}_6$ .
6. Ball milling the ( $2\text{NaBH}_4+\text{MnCl}_2$ ) mixture for 0.5 h with 5 wt. %  $\text{LiNH}_2$  almost completely eliminates the release of diborane gas,  $\text{B}_2\text{H}_6$ .

7. This addition of  $\text{LiNH}_2$  also remarkably reduces desorption temperature and accelerates desorption kinetics, and the mixture desorbs 2-3 wt. %  $\text{H}_2$  in the temperature range 100-160°C.
8. Remarkably, during the process of solvent extraction at 42°C, in order to remove NaCl-type salt from the mixture, the amorphous  $\text{a-Mn(BH}_4)_2$  transforms into its crystalline form,  $\text{c-Mn(BH}_4)_2$ .
9. Desorption of this isolated  $\text{c-Mn(BH}_4)_2$  powder also results lower diborane gas release ( $\text{H}_2/\text{B}_2\text{H}_6$  ratio in the range of 1500-1600) compared to  $\text{a-Mn(BH}_4)_2$  ( $\text{H}_2/\text{B}_2\text{H}_6$  ratio in the range of 700-900).
10. When the dead weight NaCl-type salt is removed from the mixture,  $\text{c-Mn(BH}_4)_2$  desorbs an unprecedented ~7 wt. %  $\text{H}_2$  at 100°C.

## References

- [1] D. Scott, *Smelling land : the hydrogen defense against climate catastrophe*, Canada: Canadian Hydrogen Association, 2007.
- [2] Hordeski, Michael Frank, *Hydrogen & Fuel Cells: Advances in Transportation and Power*, Fairmont Press, 2008.
- [3] R. A. Varin and A. Shirani Bidabadi, "Nanostructured, complex hydride systems for hydrogen generation," *AIMS Energy*, vol. 3, no. 1, pp. 121-143, 2015.
- [4] R. Varin, T. Czujko and Z. Wronski, *Nanomaterials for Solid State Hydrogen Storage*, New York: Springer Science, 2009.
- [5] L. Schlapbach and A. Zuttel, "Hydrogen-storage materials for mobile applications," *Nature*, vol. 414, p. 353, 2001.
- [6] S. G., "Hydrogen Storage and its Limitations," in *Interface*, The Electrochemical Society, Fall 2004, pp. 40-44.
- [7] S. Aceves, J. Martinez-Frias and O. Garcia-Villazana, "Analytical and experimental evaluation of insulated pressure vessels for cryogenic hydrogen storage," *International Journal of Hydrogen Energy*, vol. 25, no. 11, pp. 1075-1085, 2000.
- [8] S. Aceves and G. Berry, "Thermodynamics of insulated pressure vessels for vehicular hydrogen storage," *ASME Journal of Energy Resources Technology*, vol. 120, pp. 137-142, 1998.
- [9] W. Grochala and E. PP, "Thermal decomposition of the non-interstitial hydrides for the storage and production of hydrogen," *Chem. Rev.*, vol. 104, pp. 1283-1315, 2004.
- [10] "Basic Research Needs for the Hydrogen Economy," in *Basic Research Challenges for Hydrogen Storage*, Washington DC, US Department of Energy, 2004, pp. 31-51.
- [11] "Multi-Year Research, Development and Demonstration Plan," US Department of Energy, 2012. [Online]. Available: [http://energy.gov/sites/prod/files/2015/01/f19/fcto\\_myrd\\_d\\_table\\_onboard\\_h2\\_storage\\_systems\\_doe\\_targets\\_ldv.pdf](http://energy.gov/sites/prod/files/2015/01/f19/fcto_myrd_d_table_onboard_h2_storage_systems_doe_targets_ldv.pdf). [Accessed 6 July 2016].
- [12] R. Varin and A. Shirani Bidabadi, "Rapid, ambient temperature hydrogen generation from the solid state Li-B-Fe-H system by mechano-chemical activation synthesis," *Journal of Power Sources*, vol. 284, pp. 552-565, 2015.

- [13] R. Černý, N. Penin, H. Hagemann and Y. Filinchuk, "The first crystallographic and spectroscopic characterization of a 3d-metal borohydride:  $\text{Mn}(\text{BH}_4)_2$ ," *J. Phys. Chem. C*, vol. 113, pp. 9003-9007, 2009.
- [14] P. Choudhury, S. Srinivasan, V. Bhethanabotla, Y. Goswami, K. McGrath and E. K. Stefanakos, "Nano-Ni doped Li-Mn-B-H system as a new hydrogen storage candidate," *International Journal of Hydrogen Energy*, vol. 34, pp. 6325-34, 2009.
- [15] R. Varin and L. Zbronic, "The effects of ball milling and nanometric nickel additive on the hydrogen desorption from lithium borohydride and manganese chloride ( $3\text{LiBH}_4+\text{MnCl}_2$ ) mixture," *Int. J. Hydrogen Energy*, vol. 35, pp. 3588-3597, 2010.
- [16] R. Varin, L. Zbronic, M. Polanski, Y. Filinchuk and R. Černý, "Mechano-chemical synthesis of manganese borohydride ( $\text{Mn}(\text{BH}_4)_2$ ) and inverse cubic spinel ( $\text{Li}_2\text{MnCl}_4$ ) in the ( $n\text{LiBH}_4+\text{MnCl}_2$ ) ( $n=1, 2, 3, 5, 9$  and  $23$ ) mixtures and their dehydrogenation behavior," *Int. J. Hydrogen Energy*, vol. 37, pp. 16056-16069, 2012.
- [17] R. Liu, D. Reed and D. Book, "Decomposition behaviour of  $\text{Mn}(\text{BH}_4)_2$  formed by ball-milling  $\text{LiBH}_4$  and  $\text{MnCl}_2$ ," *J. Alloys Compd.*, vol. 515, pp. 32-38, 2012.
- [18] R. Varin and A. S. Bidabadi, "The effect of milling energy input during mechano-chemical activation synthesis (MCAS) of the nanocrystalline manganese borohydride ( $\text{Mn}(\text{BH}_4)_2$ ) on its thermal dehydrogenation properties," *Int. J. Hydrogen Energy*, vol. 39, pp. 11620-11632, 2014.
- [19] P. Chaudhury, V. Bhethanabotla and E. Stefanakos, "Manganese borohydride as a hydrogen storage candidate: first principle crystal structure and thermodynamic properties," *J. Phys. Chem. C*, vol. 113, pp. 13416-13424, 2009.
- [20] G. Severa, H. Hagemann, M. Longhini, J. Kaminski, T. Wesolowski and C. Jensen, "Thermal desorption, vibrational spectroscopic, and DFT computational studies of the complex manganese borohydrides  $\text{Mn}(\text{BH}_4)_2$  and  $[\text{Mn}(\text{BH}_4)_4]^{-2}$ ," *J. Phys. Chem. C*, vol. 114, pp. 15516-15521, 2010.
- [21] I. Llamas-Jansa, N. Aliouane, S. Deledda, J. Fonnelløp, C. Frommen, T. Humphries, K. Lieutenant, S. Sartori, M. Sørby and B. Hauback, "Chloride substitution by mechano-chemical reactions between  $\text{NaBH}_4$  and transition metal chlorides," *J. Alloys Compd.*, vol. 530, pp. 186-192, 2012.
- [22] Y. Nakamori, K. Miwa, A. Ninomiya, H. Li, N. Ohba, S. Towata, A. Züttel and S. Orimo, "Correlation between thermodynamical stabilities of metal borohydrides and cation electronegativities: First principle calculations and experiments," *Phys. Rev. B*, vol. 74, pp. 1-9, 2006.

- [23] Y. Nakamori, H. Li, K. Kikuchi, M. Aoki, K. Miwa, S. Towata and S. Orimo, "Thermodynamical stabilities of metal-borohydrides," *J. Alloys Compd.*, Vols. 446-447, pp. 296-300, 2007.
- [24] A. A. Guda, I. A. Pankin, A. L. Bugaeva, K. A. Lomachenko, S. A. Guda, V. P. Dmitriev and A. V. Soldatov, "X-ray absorption spectrometry determination of the products of manganese borohydride decomposition upon heating," *Bull. Russian Academy of Sciences: Physics*, vol. 79, p. 139–143, 2015.
- [25] R. Parviz and R. Varin, "Combined effects of molar ratio and ball milling energy on the phase transformations and mechanical dehydrogenation in the lithium amide-magnesium hydride ( $\text{LiNH}_2+n\text{MgH}_2$ ) ( $n=0.5-2.0$ ) nanocomposites," *Int. J. Hydrogen Energy*, vol. 38, pp. 8313-8327, 2013.
- [26] R. Varin, S. Li, Z. Wronski, O. Morozova and T. Khomenko, "The effect of sequential and continuous high-energy impact mode on the mechano-chemical synthesis of nanostructured complex hydride  $\text{Mg}_2\text{FeH}_6$ ," *J. Alloys and Compounds*, vol. 390, pp. 282-296, 2005.
- [27] G. Sandrock, K. Gross, G. Thomas, C. Jensen, D. Meeker and S. Takara, "Engineering considerations in the use of catalyzed sodium alanates for hydrogen storage," *J. Alloys Compd.*, Vols. 330-332, pp. 696-701, 2002.
- [28] T. Marks and J. Kolb, "Covalent transition metal, lanthanide, and actinide tetrahydroborate complexes," *Chemical Reviews*, vol. 77, pp. 263-293, 1977.
- [29] V. D'Anna, A. Spyratou, M. Sharma and H. Hagemann, "FT-IR spectra of inorganic borohydrides," *Spectrochimica Acta Part A: Molecular and Biomolecular Spectrometry*, vol. 128, pp. 902-906, 2014.
- [30] Université de Genève, [Online]. Available: <http://www.unige.ch/sciences/chifi/?ftirdb.html>.
- [31] T. Humphries, M. Ley, C. Frommen, K. Munroe, T. Jensen and B. Hauback, "Crystal structure and in situ decomposition of  $\text{Eu}(\text{BH}_4)_2$  and  $\text{Sm}(\text{BH}_4)_2$ ," *J. Mater. Chemistry A*, vol. 3, pp. 691-698, 2015.
- [32] A. Calik, Y. Gencer, M. Tarakci, K. Gunduz and A. Gulec, "Boriding of equiatomic Fe-Mn binary alloy," *Acta Physica Polonica*, vol. 123, pp. 449-452, 2013.
- [33] X. Meng, K. Bao, P. Zhu, Z. He, Q. Tao, J. Li, Z. Mao and T. Cui, "Manganese borides synthesized at high pressure and high temperature," *Journal of Applied Physics*, vol. 111, 2012.

- [34] R. Varin and A. Shirani Bidabadi, "Mechano-chemical activation of the (3LiBH<sub>4</sub>+TiF<sub>3</sub>) system, its dehydrogenation behavior and the effects of ultrafine filamentary Ni and graphene additives," *to be submitted for publication*, 2016.
- [35] N. Tumanov, D. Safin, B. Richter, Z. Łodziana, T. Jensen, Y. Garcia and Y. Filinchuk, "Challenges in the synthetic routes to Mn(BH<sub>4</sub>)<sub>2</sub>: insight into intermediate compounds," *Dalton Transactions*, vol. 44, pp. 6571-6580, 2015.
- [36] A. S. Bidabadi, A. Korinek, G. A. Botton and R. Varin, "High resolution transmission electron microscopy (TEM), energy-dispersive X-ray spectrometry (EDS) and X-ray diffraction studies of nanocrystalline manganese borohydride (Mn(BH<sub>4</sub>)<sub>2</sub>) after mechano-chemical synthesis and thermal dehydrogenation," *Acta materialia*, vol. 100, pp. 392-400, 2015.
- [37] R. Varin and R. Parviz, "Hydrogen generation from the ball milled composites of sodium and lithium borohydride (NaBH<sub>4</sub>/LiBH<sub>4</sub>) and magnesium hydroxide (Mg(OH)<sub>2</sub>) without and with the nanometric nickel (Ni) additive," *International Journal of Hydrogen Energy*, vol. 37, pp. 1584-1593, 2012.

## Appendix A: Conversion of Volumetric Sieverts Apparatus Measurement to wt. %

The following equation was used to convert the increase in pressure observed in the Sieverts apparatus to a corresponding measurement of the wt. % of H<sub>2</sub> desorbed by the sample in the reactor:

$$H_2 \text{ wt. \% desorbed} = \frac{\text{Mass of } H_2 \text{ desorbed}}{\text{Mass of powder}} \times 100 = \frac{2.016V}{1000RT} \times \Delta P$$

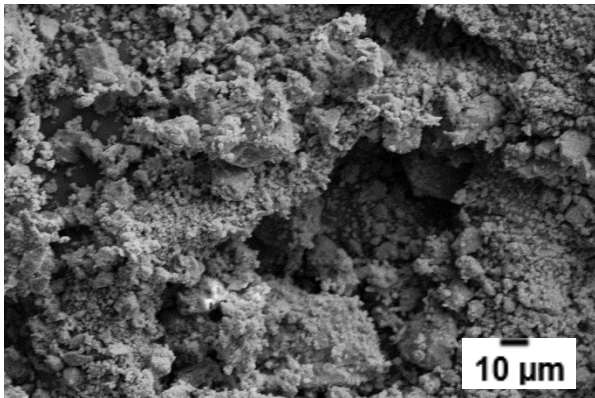
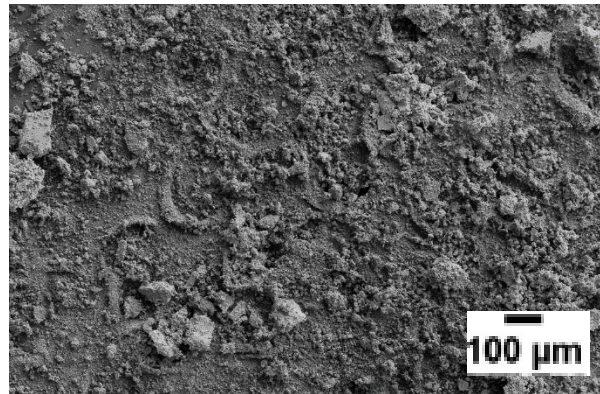
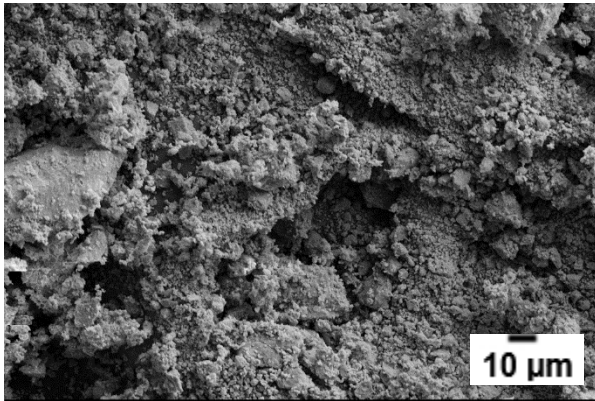
Where V = volume of system (Sieverts apparatus piping + reactor) in cm<sup>3</sup> and corrected for temperature, RT = 24.772 where R = gas constant (0.08314 m<sup>3</sup> bar K<sup>-1</sup> mol<sup>-1</sup>) and T = 298 K; ΔP = increase in gas pressure observed in the Sieverts apparatus in bar, converted from the mV reading observed on a multimeter using the following equation:

$$\Delta P = \{27.585(mV + mV_0) - 24.992\} - P_{\text{empty}}$$

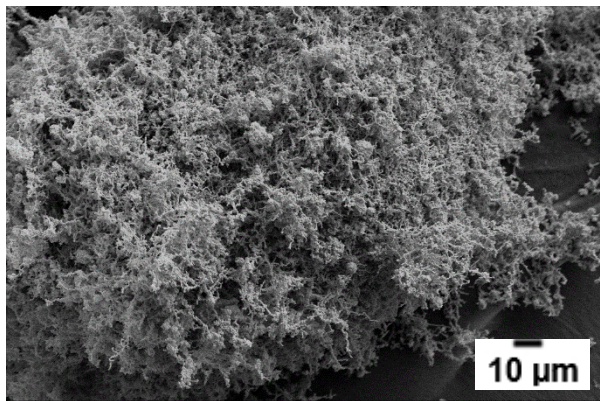
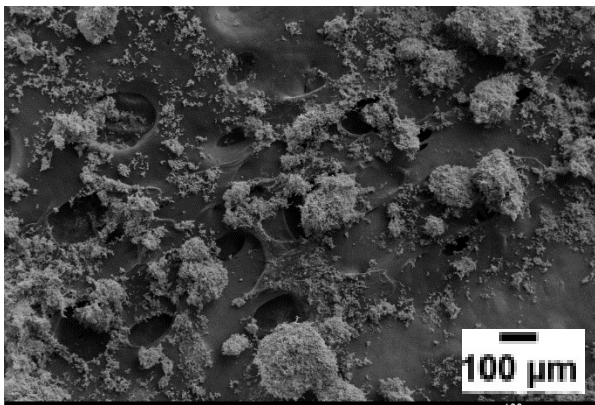
Where mV = current multimeter reading in millivolts, mV<sub>0</sub> = initial multimeter reading in millivolts and P<sub>empty</sub> = pressure of the “empty” system in bar.

## Appendix B: Collection of SEM Images

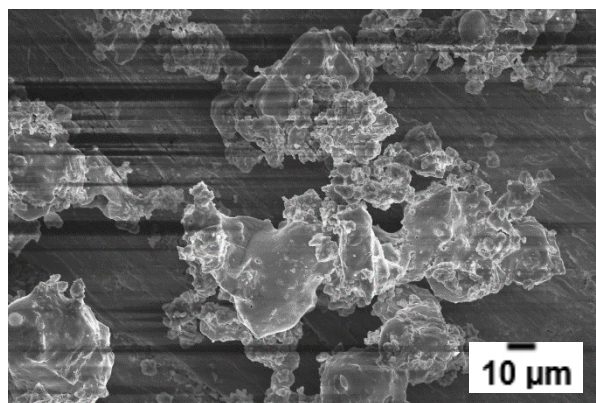
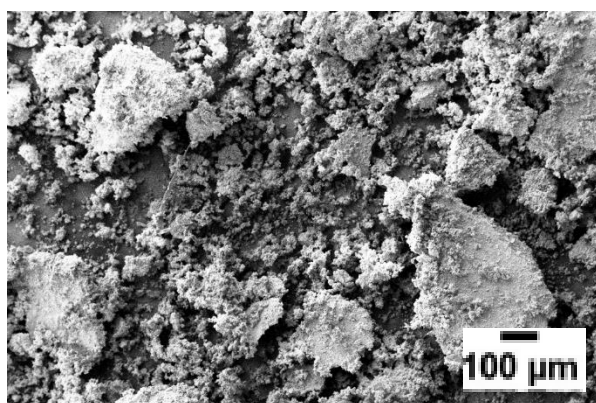
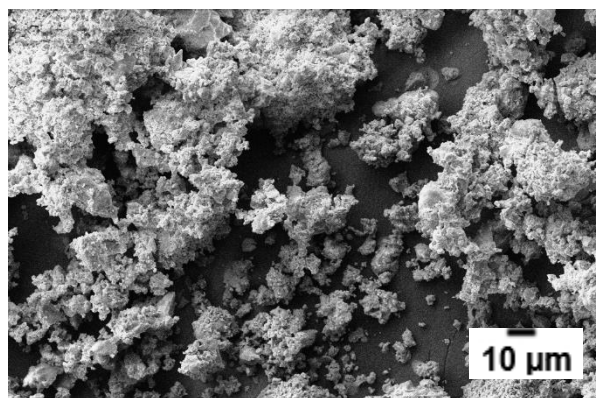
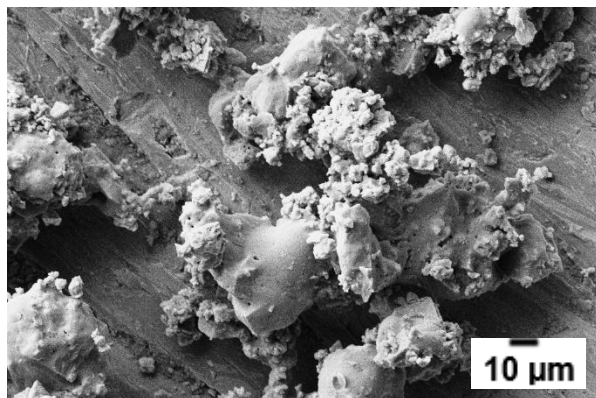
1.  $(2\text{NaBH}_4 + \text{MnCl}_2) + 5 \text{ wt. } \% \text{ Ni } 0.5 \text{ h BM}$



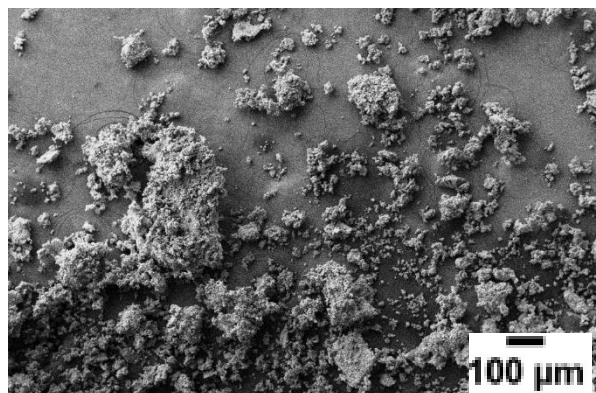
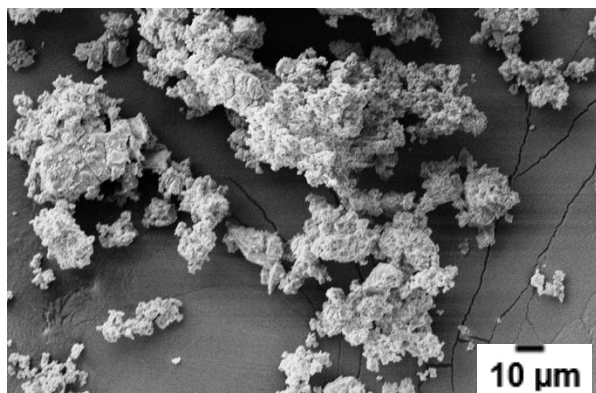
2. Pure Ni

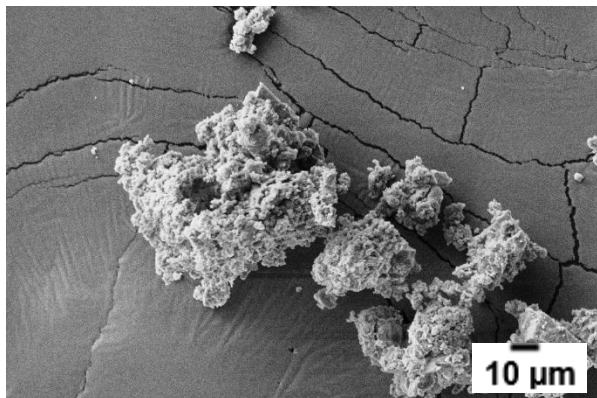


3.  $(2\text{NaBH}_4 + \text{MnCl}_2)$  5 h BM

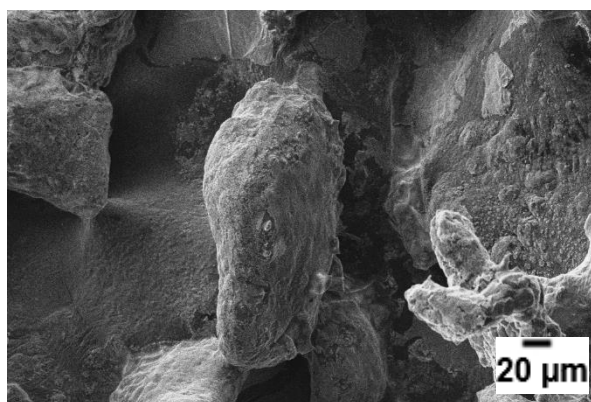
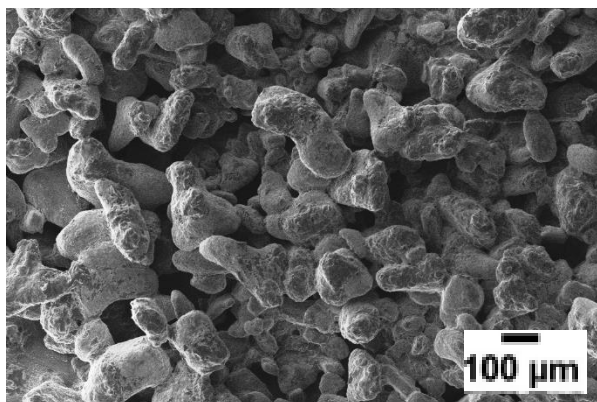
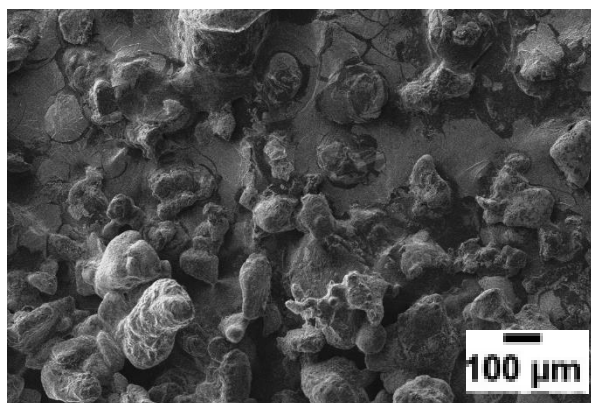
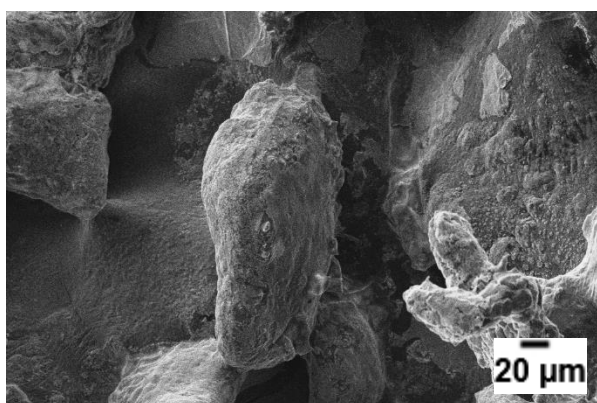


4.  $(2\text{NaBH}_4 + \text{MnCl}_2)$  0.5 h BM

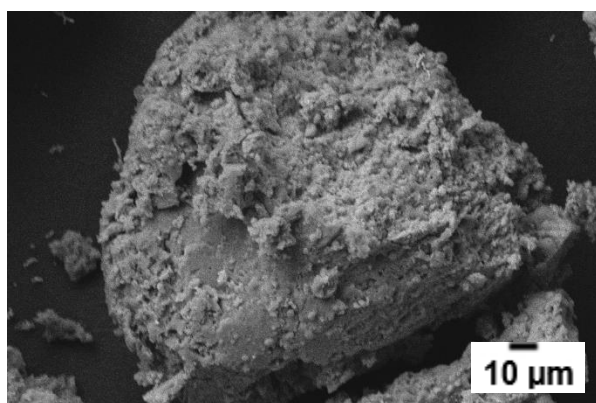
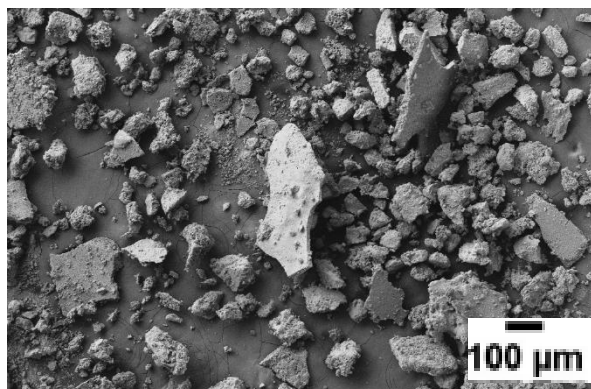
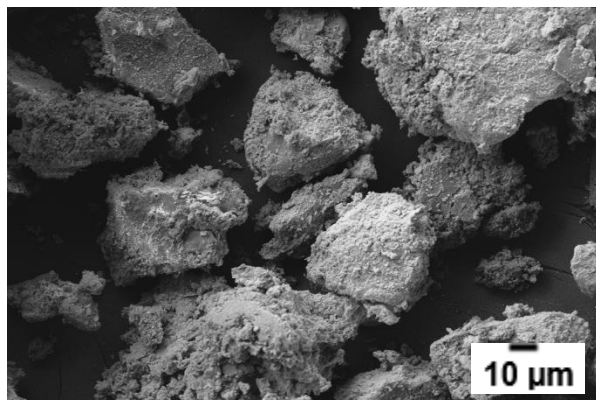




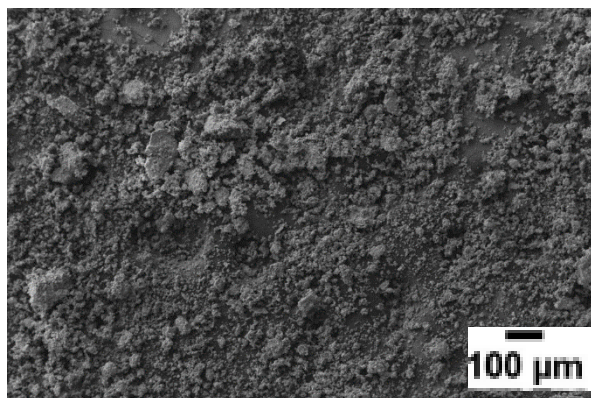
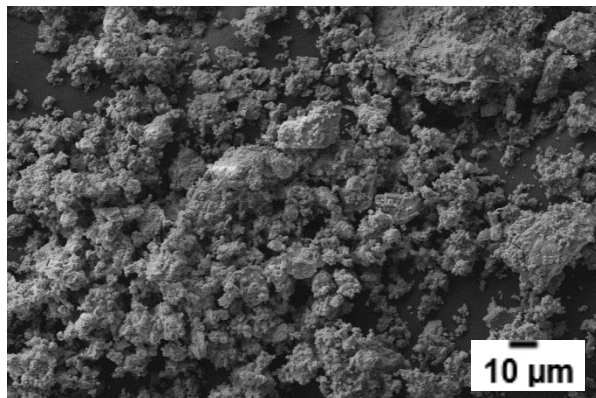
5. As received  $\text{NaBH}_4$

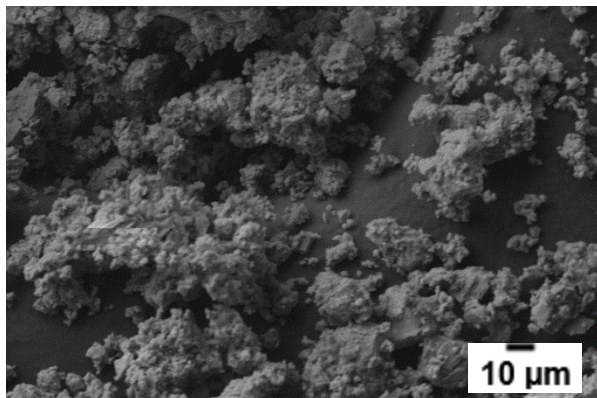


6.  $(2\text{NaBH}_4 + \text{MnCl}_2)$  1 h BM and extracted at  $42^\circ\text{C}$

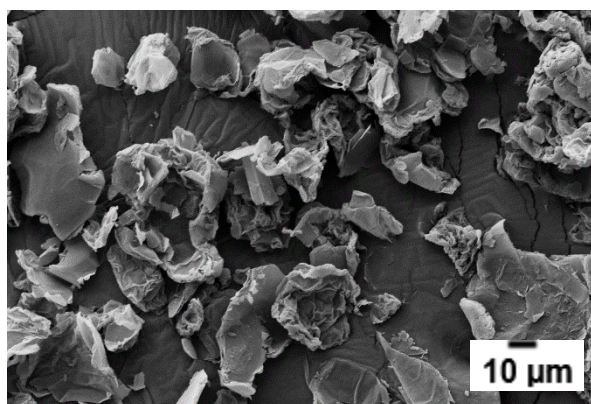
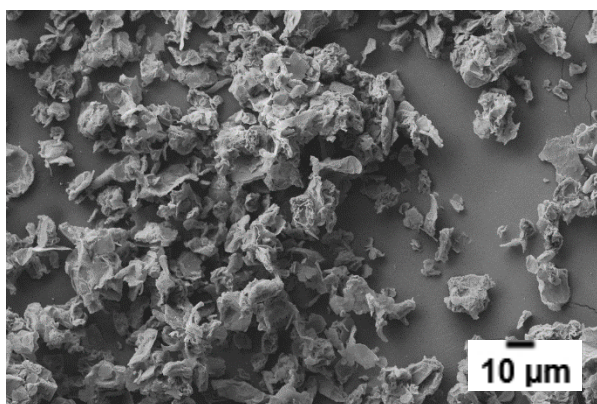
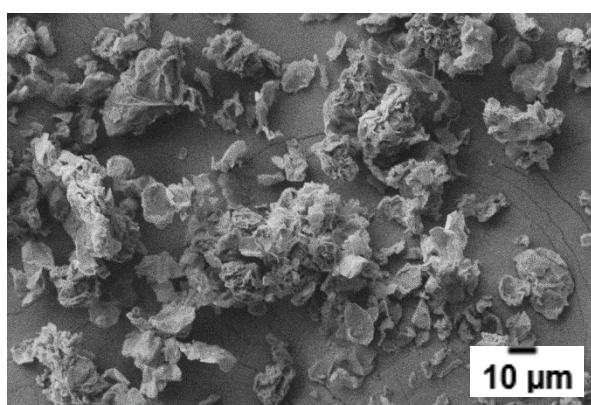
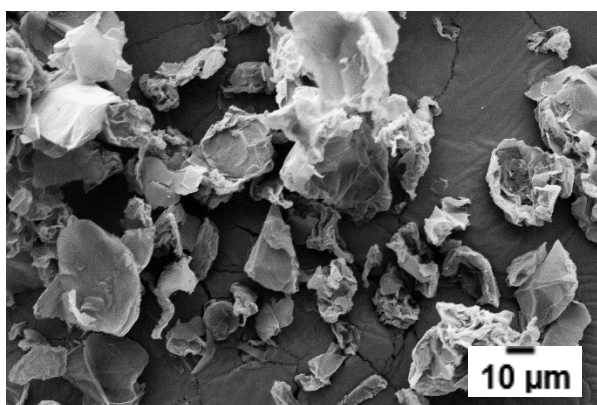


7.  $(2\text{NaBH}_4 + \text{MnCl}_2) + 5\ \text{wt. \%}$  graphene 0.5 h BM

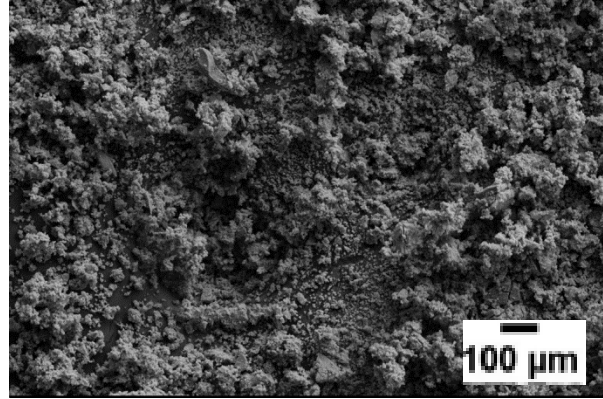
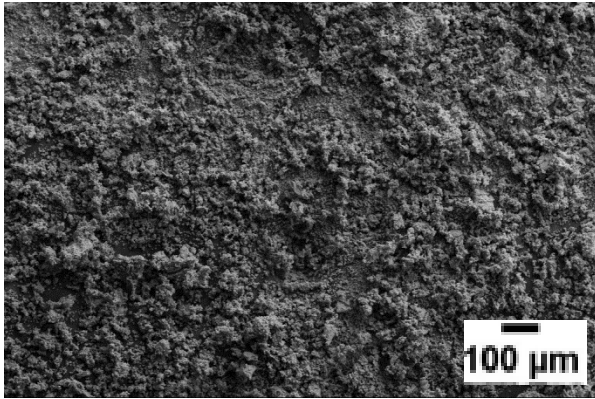




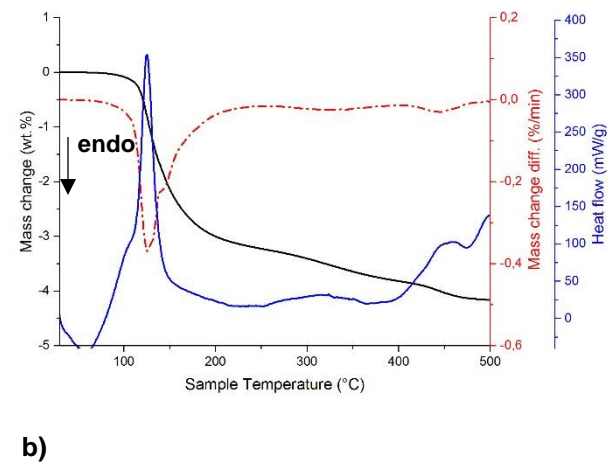
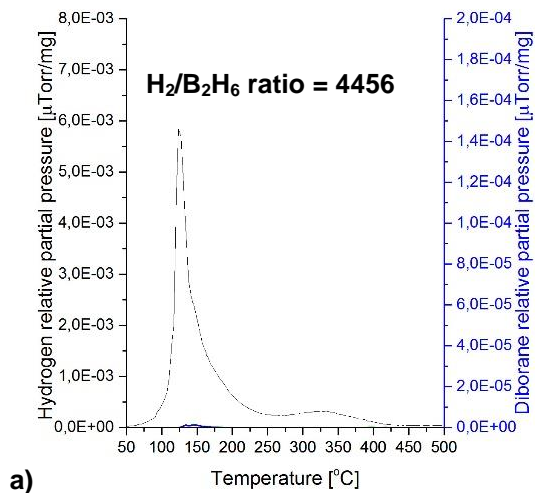
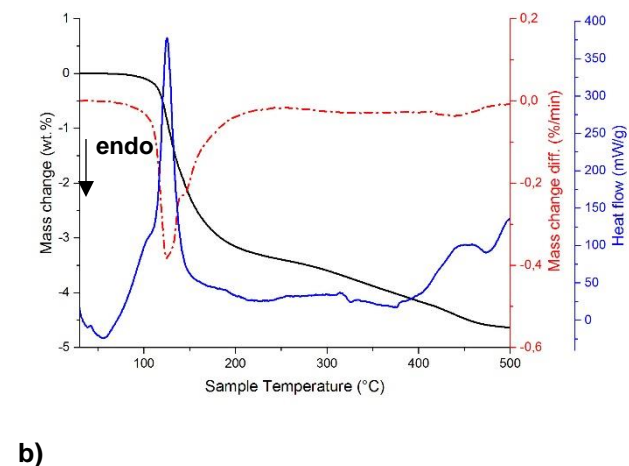
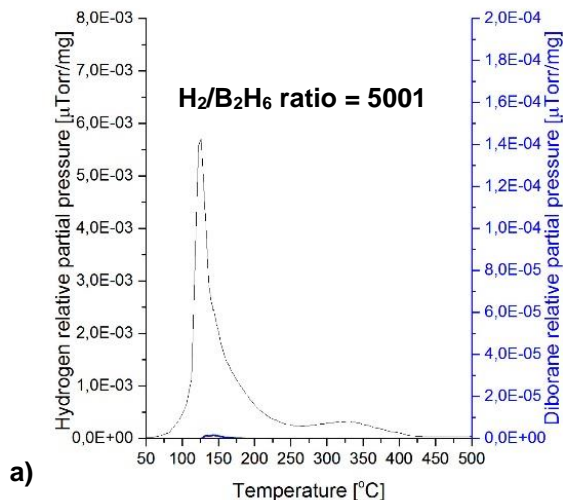
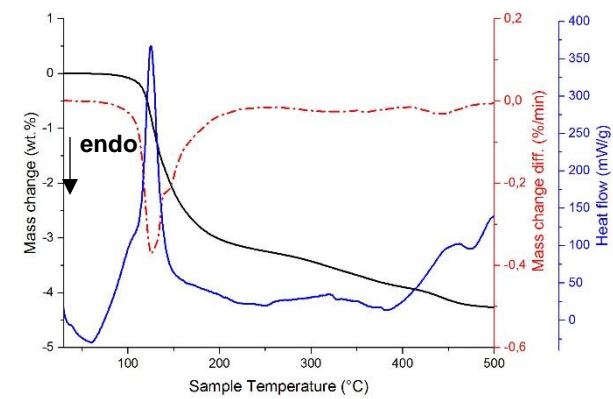
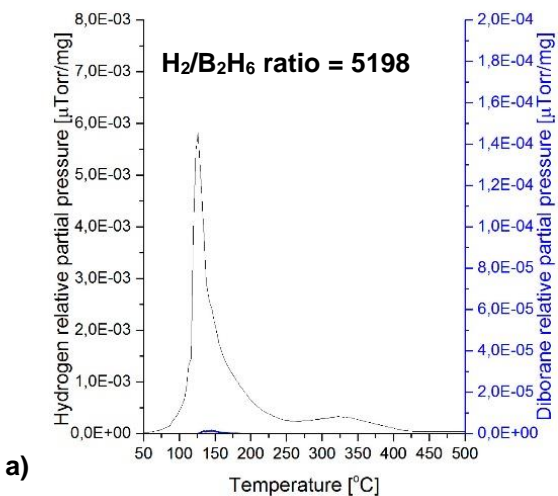
8. *Pure graphene*



9.  $(2\text{NaBH}_4 + \text{MnCl}_2) + 5 \text{ wt. \% Ni } 1 \text{ h BM}$



**Appendix C: DSC/TGA and MS data reproducibility for (2NaBH<sub>4</sub> + MnCl<sub>2</sub>) + 5 wt. % LiNH<sub>2</sub>**



## Appendix D: Enthalpy of Reactions (5) and (6)



$$\Delta H_{\text{reaction}} = \Delta H_f(\text{products}) - \Delta H_f(\text{reactants})$$

$\Delta H_f(\text{LiNH}_2) = -182 \text{ kJ/mol}$ ,  $\Delta H_f(\text{B}_2\text{H}_6) = 35.56 \text{ kJ/mol}$ ,  $\Delta H_f(\text{LiH}) = -90.63 \text{ kJ/mol}$ ,  $\Delta H_f(\text{BN}) = -254.39 \text{ kJ/mol}$ ,  $\Delta H_f(\text{LiBH}_4) = -190.46 \text{ kJ/mol}$ .

For (5),  $\Delta H_{\text{reaction}} = [2(-254.39) + 2(-90.63)] - [2(-182) + 35.56] = -361.6 \text{ kJ/mol}$

For (6),  $\Delta H_{\text{reaction}} = [(-254.39) + (-190.46)] - [(-182) + 35.56] = -298.41 \text{ kJ/mol}$ .

[AD 1] <http://www.fmclithium.com/Portals/FMCLithium/content/docs/DataSheet/QS-PDS-011%20r1.pdf> (for LiNH<sub>2</sub>)

[AD 2] <http://chemistry-reference.com/standard%20thermodynamic%20values.pdf> (for B<sub>2</sub>H<sub>6</sub>, LiH, BN and LiBH<sub>4</sub>)

**Appendix E: Hydrogen/diborane peak ratios of all samples up to 200°C**

Sample	Hydrogen/diborane peak area ratio up to 200°C
(2NaBH <sub>4</sub> +MnCl <sub>2</sub> ) 0.5 h BM – 1	735
(2NaBH <sub>4</sub> +MnCl <sub>2</sub> ) 0.5 h BM – 2	948
(2NaBH <sub>4</sub> +MnCl <sub>2</sub> ) + 5 wt % graphene 0.5 h BM – 1	1844
(2NaBH <sub>4</sub> +MnCl <sub>2</sub> ) + 5 wt % graphene 0.5 h BM – 2	1256
(2NaBH <sub>4</sub> +MnCl <sub>2</sub> ) + 5 wt % LiNH <sub>2</sub> 0.5 h BM – 1	5198
(2NaBH <sub>4</sub> +MnCl <sub>2</sub> ) + 5 wt % LiNH <sub>2</sub> 0.5 h BM – 2	5001
(2NaBH <sub>4</sub> +MnCl <sub>2</sub> ) + 5 wt % LiNH <sub>2</sub> 0.5 h BM – 3	4456
(2NaBH <sub>4</sub> +MnCl <sub>2</sub> ) 1 h BM extracted at 42°C – 1	1626
(2NaBH <sub>4</sub> +MnCl <sub>2</sub> ) 1 h BM extracted at 42°C – 2	1546

**Publications as a result of this work:**

1) R.A. Varin, **D.K. Mattar**, A.S. Bidabadi, M. Polanski; “*Synthesis of amorphous manganese borohydride, its hydrogen generation properties and crystalline transformation during solvent extraction*”, **Journal of Energy Chemistry**, accepted Aug 2016 – in press.

2) **D.K. Mattar**, A.S. Bidabadi, R.A. Varin; “*Mechano-chemical Activation Synthesis (MCAS) of Disordered Manganese Borohydride ( $d\text{-Mn}(\text{BH}_4)_2$ ) and its Nanocrystallization after Solvent Extraction*”, *Poster Presentation at the 27<sup>th</sup> Canadian Materials Science Conference (CMSC)*, Dalhousie University, Halifax, Nova Scotia, Canada (*Jun 2015*).